PNNL-14820-1

Pacific Northwest
National Laboratory
Operated by Battelle for the
U.S. Department of Energy

MASS2
Modular Aquatic Simulation System in Two Dimensions

Theory and Numerical Methods

W. A. Perkins
M. C. Richmond

September 2004

Prepared for the U.S. Department of Energy
under Contract DE-AC06-76RL01830

DISCLAIMER

United States Government. Neither the United States Government nor any agency thereof, nor Battelle Memorial Institute, nor any of their employees, makes **any warranty, express or implied, or assumes any legal liability or responsibility for the accuracy, completeness, or usefulness of any information, apparatus, product, or process disclosed, or represents that its use would not infringe privately owned rights**. Reference herein to any specific commercial product, process, or service by trade name, trademark, manufacturer, or otherwise does not necessarily constitute or imply its endorsement, recommendation, or favoring by the United States Government or any agency thereof, or Battelle Memorial Institute. The views and opinions of authors expressed herein do not necessarily state or reflect those of the United States Government or any agency thereof.

PACIFIC NORTHWEST NATIONAL LABORATORY
operated by
BATTELLE
for the
UNITED STATES DEPARTMENT OF ENERGY
under Contract DE-AC06-76RLO1830

Printed in the United States of America

Available to DOE and DOE contractors from the
Office of Scientific and Technical Information,
P.O. Box 62, Oak Ridge, TN 37831-0062;
ph: (865) 576-8401
fax: (865) 576-5728
email: reports@adonis.osti.gov

Available to the public from the National Technical Information Service,
U.S. Department of Commerce, 5285 Port Royal Rd., Springfield, VA 22161
ph: (800) 553-6847
fax: (703) 605-6900
email: orders@ntis.fedworld.gov
online ordering: http://www.ntis.gov/ordering.htm

This document was printed on recycled paper.
(8/00)

PNNL-14820-1

MASS2
Modular Aquatic Simulation System in Two Dimensions

Theory and Numerical Methods

W. A. Perkins
M. C. Richmond

September 2004

Prepared for the U.S. Department of Energy
under Contract DE-AC06-76RL01830

Pacific Northwest National Laboratory
Richland, Washington 99352

Summary

The Modular Aquatic Simulation System in Two Dimensions (MASS2) is a two-dimensional, depth-averaged hydrodynamic and transport model. The model simulates time varying distributions of depth-averaged velocities, water surface elevations, and water quality constituents. MASS2 is applicable to a wide variety of environmental analyses of rivers and estuaries where vertical variations in the water column are negligible or unimportant.

MASS2 uses a boundary-fitted, orthogonal, curvilinear computational mesh. A key feature is the use of multiple computational mesh blocks. Multiple blocks allow MASS2 to be applied to complex domains. Blocks can be connected to each other with cells having a one-to-one or one-to-many correspondence. This allows the use of a high-density mesh where detailed results are needed and coarser meshes elsewhere.

MASS2 is designed to simulate a range of river and estuarine flow and water quality problems. MASS2 can simulate a wide variety of hydrodynamic conditions, including supercritical flow and hydraulic jumps. MASS2 can also be used to simulate the fate and transport of water quality parameters. Any number of conservative or decaying scalar quantities (e.g., salinity, radionuclides) may be simulated simultaneously with hydrodynamics or using precomputed hydrodynamics. In addition, MASS2 has the ability to simulate some special water quality parameters: total dissolved gas, temperature, and suspended sediment.

The equations of mass, momentum, and species conservation are discretized using the finite-volume method and solved using iterative solution procedures. The coupling of the momentum and mass conservation (continuity) equations is achieved using a variation of the SIMPLE algorithm extended to shallow-water flows. MASS2 is coded in standard Fortran90 and has been compiled on a variety of operating systems including Linux, Windows, and Mac OS X.

Features and capabilities of MASS2 include the following:

- Fully-conservative formulation of the governing equations that allows for shock-capturing
- Unsteady simulation including time-marching to a steady-state
- Multi-block, orthogonal curvilinear computational grid to allow for simulation of complex channels and islands
- Implicit finite-volume discretization on a staggered grid
- Iterative solution methods
- Parallel processing using message passing interface (MPI)
- Subcritical flows

- Supercritical flows including hydraulic jumps
- Wetting and drying of cells
- Temperature simulation through solution of the thermal energy equation
- Total dissolved gas transport including a temperature-dependent equation of state
- Species and contaminant transport
- Non-conservative transport processes such as surface heat exchange, surface gas exchange, sediment-contaminant interaction
- Suspended sediment transport
- Bed evolution including erosion and deposition
- Sediment-contaminant interaction using partition coefficients
- Spatially-distributed coefficients (roughness, eddy viscosity, species diffusion)
- Input and model control using text files
- Restart from previous simulation results
- Transport-only model using previously computed hydrodynamics

This report documents the theory and numerical methods used in MASS2. In addition, the results of several hydrodynamic and transport validation tests are presented. A companion user manual documents the application of MASS2.

Acknowledgments

The authors would like to gratefully acknowledge the funding used to both develop and document the Modular Aquatic Simulation System in Two Dimensions (MASS2). The preparation of this document was funded by the U.S. Department of Energy (DOE) as part of the Hanford Site-Wide Assessment Project at Pacific Northwest National Laboratory (PNNL). A key aspect of this project is the System Assessment Capability (SAC), which uses MASS2 to simulate radionuclide fate and transport in the Hanford Reach of the Columbia River. The development of the MASS2 code was funded under contract with the Walla Walla and Portland Districts of the U.S. Army Corps of Engineers, and DOE.

The authors would also like to thank Chris Cook for his technical review and Sheila Bennett for her editorial review of this document. Their roles in the preparation of this document are appreciated.

Glossary of Symbols

The following is a list of the symbols and their definitions used in this document. Where specific units are required, those units are listed with the definition of the symbol. However, most of the theory presented in this document is applicable in any consistent set of units. So in lieu of specific units, dimensions are listed in square brackets ([]). Dimensions are abbreviated as follows: M = mass, L = length, T = time, and F = force (= MLT^{-2}).

α	solar altitude (radians)
α_d	depth correction under-relaxation factor
β_{air}	apparent Bunsen coefficient for air (L/L·atm)
β_i	Bunsen coefficient for gas fraction *i* (L/L·atm)
δ	declination of the sun (radians)
Δt	time step [T]
λ_ϕ	decay rate of transported scalar ϕ [T^{-1}]
(ξ, η)	orthogonal computational coordinates
ρ	fluid density [ML^{-3}]
ρ_b	bed bulk density[ML^{-3}]
ρ_{s_j}	solids density sediment fraction *j* [ML^{-3}]
σ^*	Stephan-Boltzmann constant (5.67×10^{-8} W/m^{2}K^4)
τ_b	bottom shear stress [FL^{-2}]
τ_{b_1}	bottom shear stress component in the ξ-direction [FL^{-2}]
τ_{b_2}	bottom shear stress component in the η-direction [FL^{-2}]
τ_{d_j}	bottom shear stress below which deposition of sediment fraction *j* occurs [FL^{-2}]
τ_{e_j}	bottom shear stress above which erosion of sediment fraction *j* is initiated [FL^{-2}]
τ_{s_1}	surface shear stress component in the ξ-direction [FL^{-2}]
τ_{s_2}	surface shear stress component in the η-direction [FL^{-2}]
ε_1	turbulent diffusion coefficient in the ξ-direction [L^{2}T^{-1}]
ε_2	turbulent diffusion coefficient in the η-direction [L^{2}T^{-1}]
ε_t	turbulent diffusion coefficient [L^{2}T^{-1}]
ε_w	emissivity of water (0.97)
ϕ	volumetric concentration of a dissolved transported scalar [ML^{-3}]
Φ	site latitude (radians)
ϕ_{bed_j}	concentration of particulate contaminant sorbed to sediment fraction *j* in the bed, per unit sediment mass [MM^{-1}]
ϕ_{part_j}	volumetric concentration of the particulate phase of scalar ϕ associated with sediment fraction *j* [ML^{-3}]
ϕ_{pore}	volumetric concentration of scalar quantity ϕ in the bed pore water [ML^{-3}]
ϕ_{sed_j}	volumetric concentration of sediment fraction *j* suspended in the water column [ML^{-3}]
a_t	short-wave radiation atmospheric transmission coefficient

A_{air}	apparent molecular volume of air (with unit conversion, atm·L/mg·mm Hg)
a_w	wind function coefficient (W/m^2/mm Hg)
b_w	wind function coefficient (W·sec^2/mm Hg)
C	total dissolved gas concentration (mg/L)
C_*	saturation concentration of air at the water surface (mg/L)
C_a	Brunt's coefficient
C_L	cloudiness as a fraction of sky covered
c_v	specific heat of water at 15°C (4186 J/kg·°C)
d	water depth [L]
D_{50_j}	median particle diameter of sediment fraction j [L]
d_{bed}	bed depth [L]
D_j	deposition rate of sediment fraction j [ML^{-2}T^{-1}]
D_{pore_ϕ}	diffusion rate of scalar quantity ϕ between the water column and bed pore water [L^{2}T^{-1}]
E	equation of time (hr)
E_{o_j}	erodibility coefficient for sediment fraction j [ML^{-2}T^{-1}]
E_j	erosion rate of sediment fraction j [ML^{-2}T^{-1}]
e_a	actual water vapor pressure in air (mm Hg)
e_s	water vapor saturation pressure of air at the water surface (mm Hg)
F_j	fraction of sediment fraction j in the bed [MM^{-1}]
g	gravitational constant [LT^{-2}]
g_{11}	metric coefficient [L^2]
g_{21}, g_{12}	metric coefficient [L^2]
g_{22}	metric coefficient [L^2]
h	hour angle of the sun (radians)
h_1	metric coefficient in the ξ direction [L]
h_2	metric coefficient in the η direction [L]
H_a	measured incoming short-wave solar radiation (W/m^2)
H_{an}	net atmospheric long-wave radiation at the water surface (W/m^2)
H_b	long-wave back-radiation at the water surface (W/m^2)
H_e	heat flux at the water surface due to evaporation (W/m^2)
H_c	heat flux at the water surface due to conduction (W/m^2)
H_o	radiation flux reaching the earth's atmosphere (W/m^2)
H_{sn}	net incoming solar short-wave radiation at the water surface (W/m^2)
K_{ϕ_j}	rate of mass transfer between dissolved and particulate phases of scalar ϕ [T^{-1}]
$K_{b_{\phi_j}}$	coefficient defining partitioning of scalar quantity ϕ between dissolved and particulate sorbed to sediment fraction j in the bed [L^{3}M^{-1}]
$K_{d_{\phi_j}}$	coefficient defining partitioning of scalar quantity between dissolved and particulate sorbed to sediment fraction j [L^{3}M^{-1}]
K_L	dissolved gas surface transfer coefficient [MT^{-1}]
L_{loc}	site longitude (radians)
L_{st}	standard longitude for the local time zone (radians)

$M_{\phi_{\mathrm{bed}}}$	total mass (all phases) of scalar ϕ in the bed per unit bed area [ML^{-2}]
$M_{\phi_{\mathrm{bed}_j}}$	mass of particulate ϕ sorbed to sediment fraction j per unit bed area [ML^{-2}]
$M_{\phi_{\mathrm{pore}}}$	mass of scalar ϕ per unit bed area within the bed pore water [ML^{-2}]
M_{bed}	total mass of sediment in the bed per unit bed area [ML^{-2}]
M_{sed_j}	mass of sediment fraction j in the bed per unit bed area [ML^{-2}]
N_{sed}	number of sediment fractions
p	bed porosity
$P_{\mathrm{H_20}}$	vapor pressure of water (mm Hg)
P_{TDG}	total dissolved gas pressure (mm Hg)
R_s	albedo or reflection coefficient
S_ϕ	source term for the transport equation when dissolved scalar ϕ is represented [ML^{-2}T^{-1}]
$S_{\phi_{\mathrm{part}_j}}$	source term for the transport equation when the particulate phase of scalar ϕ sorbed to sediment fraction j is represented [ML^{-2}T^{-1}]
S_{sed_j}	source term for the transport equation when suspended sediment fraction j is represented [ML^{-2}T^{-1}]
S_T	source term for the scalar transport equation when thermal energy transport is represented
t	time [T]
T	water temperature (°C)
$t_{\phi_{1/2}}$	half-life of transported scalar ϕ [T]
T_{11}, T_{21}, T_{22}	components of the effective stress tensor [FL^{-2}]
T_a	air temperature (°C)
t_l	local time (hr)
t_s	solar time (hr)
u	depth-averaged velocity component in the x-direction [LT^{-1}]
U	depth-averaged velocity component in the ξ-direction [LT^{-1}]
v	depth-averaged velocity component in the y-direction [LT^{-1}]
V	depth-averaged velocity component in the η-direction [LT^{-1}]
w_j	settling velocity of sediment fraction j in water [LT^{-1}]
W	wind speed [LT^{-1}]
X_i	mole fraction of gas i
x, y	Cartesian physical coordinates, e.g., state plane coordinates [L]
z_b	bottom elevation [L]

Contents

Summary iii

Acknowledgments v

Glossary of Symbols vii

1 Introduction 1

2 Model Theory 3

- 2.1 Coordinates and Grid System 3
- 2.2 Hydrodynamics 4
- 2.3 Scalar Transport 6
  - 2.3.1 Dissolved Scalar Source Term 6
  - 2.3.2 Suspended Sediment Source Term 7
  - 2.3.3 Particulate Scalar Source Term 8
  - 2.3.4 Thermal Energy (Temperature) Source Term 8
  - 2.3.5 Total Dissolved Gas 10

3 Numerical Methods 13

- 3.1 Computational Mesh 13
- 3.2 Discrete Forms of Governing Equations 13
  - 3.2.1 Discretized Form of the General Scalar Transport Equation 15
  - 3.2.2 Discretized Form of the Momentum Equations 17
  - 3.2.3 Velocity-Depth Coupling 18
- 3.3 Solution Procedure 20

3.3.1 Hydrodynamics 20

3.3.2 Scalar Transport 22

3.4 Initial Conditions 25

3.5 Boundary Conditions 25

3.6 Mesh Block Connections 28

3.7 Wetting and Drying 29

3.8 Bed Accounting 30

3.8.1 Sediment 30

3.8.2 Transported Scalars 30

4 Validation Tests 35

4.1 Hydrodynamic Tests 35

4.1.1 Subcritical, Uniform Flow in a Rectangular Channel 35

4.1.2 Subcritical, Uniform Flow in a Trapezoidal Channel 36

4.1.3 Gradually Varied Subcritical Flow in a Rectangular Channel 38

4.1.4 Transition to Supercritical Flow in a Rectangular Channel 39

4.1.5 Hydraulic Jump in a Straight Channel 40

4.1.6 Varied Flow in a Trapezoidal Channel 40

4.1.7 Flow in a Converging and Diverging Channel 43

4.1.8 Two-Dimensional Flow Around a Spur Dike 44

4.1.9 Side Discharge into an Open Channel 47

4.1.10 Flow in a Meandering Channel 47

4.2 General Scalar Transport Tests 50

4.2.1 One-Dimensional Advection 50

4.2.2 One-Dimensional Advective Diffusion 50

4.2.3 Lateral Mixing 53

4.2.4 Point Source 53

4.2.5 Radioactive Decay 55

4.2.6 Dissolved/Particulate Species Partitioning 56

5 Future Development 59

6 References 61

Figures

3.1 Layout of the MASS2 computational mesh for a single block. 14

3.2 Solution algorithm flow chart. 21

3.3 Hydrodynamic solution algorithm flow chart. 23

3.4 Scalar transport solution algorithm flow chart. 24

3.5 Cells computed near an open block boundary. 26

3.6 Example computational mesh block interface. 29

4.1 Profile dimensions of channel used for subcritical uniform flow in a channel flow test. 35

4.2 Simulated steady-state depth profiles from the subcritical uniform flow in a channel tests. 36

4.3 Simulated steady-state water surface elevation profiles from the subcritical uniform flow in a rectangular channel tests. 37

4.4 Channel cross section used for the uniform flow in a trapezoidal channel test. . . . 37

4.5 Comparison of simulated depth (a) and water surface elevation (b) from the subcritical, uniform flow in a trapezoidal channel. 38

4.6 Dimensions of channel used for the gradually varying flow in a channel tests. . . . 38

4.7 Simulated steady-state depths and water surface elevations from the gradually varied flow in a rectangular channel test. 39

4.8 Simulated steady-state water surface elevation and depth from the transition to supercritical flow in a rectangular channel test. 40

4.9 Simulated depth from the hydraulic jump in a straight channel test compared to that observed by Gharangik (1988). 41

4.10 Simulated water surface elevation and depth compared with the analytic solution to problem 3 of MacDonald et al. (1997). 42

4.11 Simulated water surface elevation and depth compared with the analytic solution to problem 4 of MacDonald et al. (1997). 43

4.12 Model domain used to represent the converging and diverging channel test. 43

4.13 Simulated depth and velocity in the converging and diverging channel test compared with that observed by Panagiotopoulos and Soulis (2000). 44

4.14 Computational domain for the flow around a spur-dike test. 45

4.15 Streamlines from the flow around a spur dike test. 45

4.16 Simulated velocity vectors near the spur-dike. 45

4.17 Comparison of simulated velocity with observed and other reported simulations of the flow around a spur-dike test. 46

4.18 Model domain and boundary conditions for the side discharge into an open channel test. 47

4.19 Simulation results from the side discharge into an open channel test. 48

4.20 Dimensions of the simulation domain used in the meandering channel test. 48

4.21 Simulated velocity vectors in the meandering channel test case. 49

4.22 Comparison of simulated and observed velocity at the sample sections in the flow in a meandering channel test. 49

4.23 Upstream concentration boundary condition used for 1-D advection test. 51

4.24 Results of the one-dimensional advection test for three Courant numbers: (a) 0.1, (b) 1.0, and (c) 6.0. 51

4.25 Simulated concentration compared with the analytic solution to the one-dimensional advective diffusion test. 52

4.26 Concentration from multi-block simulations (points) compared to the analytic solution (equation 4.4, solid line) to the one-dimensional advective diffusion test. . . 53

4.27 Contour plot of simulated concentration from the lateral mixing test. 54

4.28 Lateral variation of simulated concentration compared with the analytic solution to the lateral mixing test. 54

4.29 Longitudinal variation of simulated concentration compared with the analytic solution to the lateral mixing test. 54

4.30 Contour plot of simulated concentration from the point source transport test. 55

4.31 Lateral (a) and longitudinal (b) variation of simulated concentration compared with the analytic solution to the point source test. 56

4.32 Simulated concentrations of a decaying scalar quantity compared with analytic solution. 57

4.33 Simulated dissolved and particulate concentrations in the species partitioning test. . 57

Tables

2.1 Gas fractions used to compute gas mass concentrations from gas pressures (Colt 1984). 11

1.0 Introduction

The Modular Aquatic Simulation System in Two Dimensions (MASS2) is a two-dimensional, depth-averaged hydrodynamic and transport model. The model simulates time varying distributions of depth-averaged velocities, water surface elevations, and water quality constituents. MASS2 was originally developed to simulate the transport and fate of total dissolved gas generated at spillways of dams on the Lower Columbia and Snake Rivers (Richmond et al. 1999b, 2000). Following its initial development, the MASS2 code has evolved to include new capabilities and has been used in a variety of investigations. Examples include studies of sediment mobility in the Lower Snake River (Richmond et al. 1999a), time-varying juvenile chinook salmon habitat along the Hanford Reach of the Columbia River (McMichael et al. 2003; Perkins et al. 2004); and the fate of Hanford Site radionuclides should they enter the Columbia River (Kincaid et al. 2001).

MASS2 uses a structured, multi-block, boundary-fitted, curvilinear computational mesh that allows the simulation of very complex riverine or estuarine networks. A single block consists of a logically rectangular computational mesh. Several blocks may be connected together. The mesh blocks may have varying resolution allowing high resolution to be used only in areas where it is needed.

MASS2 can simulate a wide variety of hydrodynamic conditions, including supercritical flow and hydraulic jumps. It can also simulate a wide variety of water quality conditions, including sediment, conservative or decaying contaminants, sediment-sorbed contaminants, water temperature, and total dissolved gas.

Any number of these constituents may be simulated simultaneously subject to the limitation of available computer memory. In addition, transport simulations may be performed using pre-calculated hydrodynamic conditions, allowing long-term transport simulations unencumbered by the more intensive hydrodynamic calculations, or repeated transport simulations without re-simulating hydrodynamics.

Capabilities and features of MASS2 include:

- Fully-conservative formulation of the governing equations that allows for shock-capturing
- Unsteady simulation including time-marching to a steady-state
- Multi-block, orthogonal curvilinear computational grid to allow for simulation of complex channels and islands
- Implicit finite-volume discretization on a staggered grid
- Iterative solution methods
- Parallel processing using message passing interface (MPI)

- Subcritical flows
- Supercritical flows including hydraulic jumps
- Wetting and drying of cells
- Temperature simulation through solution of the thermal energy equation
- Total dissolved gas transport including a temperature-dependent equation of state
- Species and contaminant transport
- Non-conservative transport processes such as surface heat exchange, surface gas exchange, sediment-contaminant interaction
- Suspended sediment transport
- Bed evolution including erosion and deposition
- Sediment-contaminant interaction using partition coefficients
- Spatially-distributed coefficients (roughness, eddy viscosity, species diffusion)
- Input and model control using text files
- Restart from previous simulation results
- Transport-only model using previously computed hydrodynamics

MASS2 is coded in standard Fortran90 and has been compiled on a variety of operating systems including Linux, Windows, and Mac OS X.

This report documents the theory (Chapter 2) and numerical methods (Chapter 3) used in MASS2. In addition, the results are presented from several of hydrodynamic (Section 4.1) and transport (Section 4.2) validation tests to which MASS2 was subjected. The companion user manual (Perkins and Richmond 2004) documents the application of MASS2.

2.0 Model Theory

2.1 Coordinates and Grid System

The Modular Aquatic Simulation System in two-dimensions (MASS2) is formulated using an orthogonal, curvilinear coordinate system. The governing equations are formulated in conservative form using a full transformation to the curvilinear system where the velocities are the physical contravariant velocities components (Richmond et al. 1986).

The physical coordinate system is Cartesian and the metric coefficients which define the coordinate transformation take the form

$$h_1 = \sqrt{\left(\frac{\partial x}{\partial \xi}\right)^2 + \left(\frac{\partial y}{\partial \xi}\right)^2}$$

and

$$h_2 = \sqrt{\left(\frac{\partial x}{\partial \eta}\right)^2 + \left(\frac{\partial y}{\partial \eta}\right)^2}$$

where h_1 and h_2 are the metric coefficients in the ξ and η direction, (x,y) are the physical (Cartesian) coordinates, i.e., state plane coordinates, and (ξ,η) are the orthogonal computational coordinates.

Physical contravariant velocity components are the dependent variables used in the MASS2 depth-averaged momentum equations. The contravariant components have base vectors (covariant base vectors) that are tangent to the computational coordinate direction. Thus, these components "follow" the coordinate lines in the numerically generated computational grid. The physical components of a contravariant vector, denoted by $A(i)$, are determined by its projection onto the coordinate direction:

$$A(i) = A^i \mathbf{a_i} \cdot \mathbf{e_i} = \sqrt{g_{ii}} A^i \mathbf{e_i} \cdot \mathbf{e_i} = \sqrt{g_{ii}} A^i$$

To convert the physical contravariant components to a Cartesian coordinate system (e.g., for output to plotting software) the following transformation is used

$$\begin{aligned} u &= \frac{U}{\sqrt{g_{11}}}\frac{\partial x}{\partial \xi} + \frac{V}{\sqrt{g_{22}}}\frac{\partial x}{\partial \eta} \\ v &= \frac{U}{\sqrt{g_{11}}}\frac{\partial y}{\partial \xi} + \frac{V}{\sqrt{g_{22}}}\frac{\partial y}{\partial \eta} \end{aligned}$$

To convert from Cartesian coordinates to the physical contravariant coordinates:

$$\begin{aligned} U &= (u\frac{\partial \xi}{\partial x} + v\frac{\partial \xi}{\partial y})\sqrt{g_{11}} \\ V &= (u\frac{\partial \eta}{\partial x} + v\frac{\partial \eta}{\partial y})\sqrt{g_{22}} \end{aligned}$$

where u and v are the Cartesian velocity components in the x and y directions, respectively, and U and V are the physical contravariant velocity components in the η and ξ directions, respectively. The coordinate transformation is given by

$$\begin{aligned}
\frac{\partial \xi}{\partial x} &= \frac{1}{J}\frac{\partial y}{\partial \eta} \\
\frac{\partial \xi}{\partial y} &= \frac{-1}{J}\frac{\partial x}{\partial \eta} \\
\frac{\partial \eta}{\partial x} &= \frac{-1}{J}\frac{\partial y}{\partial \xi} \\
\frac{\partial \eta}{\partial y} &= \frac{1}{J}\frac{\partial x}{\partial \xi}
\end{aligned}$$

so that the physical contravariant components are

$$\begin{aligned}
U &= (u\frac{\partial y}{\partial \eta} - v\frac{\partial x}{\partial \eta})\frac{\sqrt{g_{11}}}{J} \\
V &= (-u\frac{\partial y}{\partial \xi} + v\frac{\partial x}{\partial \xi})\frac{\sqrt{g_{22}}}{J}
\end{aligned}$$

where

$$\begin{aligned}
g_{11} &= h_1^2 \\
g_{22} &= h_2^2 \\
g_{12} &= g_{21} \\
&= \frac{\partial x}{\partial \xi}\frac{\partial x}{\partial \eta} + \frac{\partial y}{\partial \xi}\frac{\partial y}{\partial \eta} \\
J &= \text{is the determinant of the Jacobian matrix} \\
&= g_{11}g_{22} - g_{12}g_{21}.
\end{aligned}$$

2.2 Hydrodynamics

The depth-averaged conservation of mass, or continuity, equation in computational coordinates is

$$h_1 h_2 \frac{\partial d}{\partial t} + \frac{\partial (h_2 d U)}{\partial \xi} + \frac{\partial (h_1 d V)}{\partial \eta} = q_s \tag{2.1}$$

where d is water depth, U is the depth-averaged velocity component in the ξ direction, V depth-averaged velocity component in the η direction, and q_s is the total of other sources.

The equation for U or ξ-direction momentum in the computational coordinates is

$$\begin{aligned}
h_1 h_2 \frac{\partial (dU)}{\partial t} + \frac{\partial \left(d h_2 U^2\right)}{\partial \xi} + \frac{\partial (d h_1 V U)}{\partial \eta} + d\frac{\partial h_1}{\partial \eta} UV - d\frac{\partial h_2}{\partial \xi} V^2 = -g h_2 d \frac{\partial (z_b + d)}{\partial \xi} \\
+ \frac{1}{\rho}\frac{\partial (d h_2 T_{11})}{\partial \xi} + \frac{1}{\rho}\frac{\partial (d h_1 T_{21})}{\partial \eta} + \frac{d}{\rho}\frac{\partial h_1}{\partial \eta} T_{21} - \frac{d}{\rho}\frac{\partial h_2}{\partial \xi} T_{22} + \frac{h_1 h_2}{\rho}\left(\tau_{s_1} - \tau_{b_1}\right)
\end{aligned} \tag{2.2}$$

where z_b is the channel bottom elevation, τ_{b_1} is the component of bottom shear stress in the ξ-direction, and τ_{s_1} is the component of surface shear stress in the ξ-direction.

Similarly, the V or η-direction momentum equation in computational coordinates is

$$\begin{aligned}h_1 h_2 \frac{\partial (dV)}{\partial t} + \frac{\partial (dh_2 UV)}{\partial \xi} + \frac{\partial \left(dh_1 V^2\right)}{\partial \eta} + d\frac{\partial h_2}{\partial \xi} UV - d\frac{\partial h_1}{\partial \eta} U^2 = -gh_1 d \frac{\partial (z_b + d)}{\partial \eta} \\ + \frac{1}{\rho}\frac{\partial (dh_2 T_{12})}{\partial \xi} + \frac{1}{\rho}\frac{\partial (dh_1 T_{22})}{\partial \eta} + \frac{d}{\rho}\frac{\partial h_2}{\partial \xi} T_{12} - \frac{d}{\rho}\frac{\partial h_2}{\partial \eta} T_{11} + \frac{h_1 h_2}{\rho}\left(\tau_{s_2} - \tau_{b_2}\right)\end{aligned} \tag{2.3}$$

where τ_{b_2} and τ_{s_2} are the bottom and surface shear stress in the η direction. The components of the stress tensor, T_{11}, T_{21}, T_{22}, are the so-called effective stresses, and these are linearly related to the fluid strain rate in an incompressible fluid through the following equations:

$$\begin{aligned}T_{11} =& 2\mu e_\xi e_\xi \\ T_{22} =& 2\mu e_\eta e_\eta \\ T_{12} =& T_{21} = \mu e_\xi e_\eta\end{aligned} \tag{2.4}$$

where

$$\begin{aligned}e_\xi e_\xi =& \frac{1}{h_1}\frac{\partial U}{\partial \xi} + \frac{V}{h_1 h_2}\frac{\partial h_1}{\partial \eta} \\ e_\eta e_\eta =& \frac{1}{h_2}\frac{\partial V}{\partial \eta} + \frac{U}{h_1 h_2}\frac{\partial h_2}{\partial \xi}\end{aligned}$$

and

$$e_\xi e_\eta = \frac{h_2}{h_1}\frac{\partial}{\partial \xi}\left(\frac{V}{h_2}\right) + \frac{h_1}{h_2}\frac{\partial}{\partial \eta}\left(\frac{U}{h_1}\right)$$

MASS2 uses the Bousinessq eddy viscosity model to represent the turbulence stresses, so the viscosity coefficient in equation 2.4 is a turbulent eddy viscosity.

Bottom shear stress is computed using

$$\tau_{b1} = \rho C_b U \sqrt{U^2 + V^2} \tag{2.5}$$

and

$$\tau_{b2} = \rho C_b V \sqrt{U^2 + V^2} \tag{2.6}$$

where the bed-friction coefficient is calculated based on the Manning roughness value, n, as

$$C_b = g\left(\frac{n^2}{1.49 d^{1/3}}\right) \tag{2.7}$$

2.3 Scalar Transport

The governing equation for the transport of a scalar is obtained by applying the principle of conservation of mass to a fluid element. In orthogonal curvilinear coordinates, the governing equation is

$$h_1 h_2 \frac{\partial (d\phi)}{\partial t} + \frac{\partial (h_2 dU\phi)}{\partial \xi} + \frac{\partial (h_1 dV\phi)}{\partial \eta} = \frac{\partial}{\partial \xi}\left(h_2 \frac{\varepsilon_1}{h_1} d \frac{\partial \phi}{\partial \xi}\right) + \frac{\partial}{\partial \eta}\left(h_1 \frac{\varepsilon_2}{h_2} d \frac{\partial \phi}{\partial \eta}\right) + h_1 h_2 S_\phi \tag{2.8}$$

where ϕ is (usually) the volumetric scalar concentration, ε_1 is the turbulent diffusion coefficient in the ξ-direction, ε_2 is the turbulent diffusion coefficient in the η-direction, and S_ϕ is the source term.

Equation 2.8 is used to represent the fate and transport of various kinds of scalar quantities. The representation of individual scalar quantities differs only in the computation of the source term, S_ϕ. The remainder of this section describes S_ϕ for specific types scalar quantities.

2.3.1 Dissolved Scalar Source Term

When equation 2.9 is used to represent the fate and transport of generic dissolved scalar quantities, the source term is

$$\begin{aligned} S_\phi = & -\lambda_\phi \phi d \\ & + \sum_{j=1}^{N_{\text{sed}}} K_{\phi_j}\left(K_{d_{\phi_j}} \phi_{\text{sed}_j} \phi - \phi_{\text{part}_j}\right) \\ & + \sum_{j=1}^{N_{\text{sed}}} \rho_{s_j} D_{50_j} (1-n) K_{\phi_j}\left(K_{b_{\phi_j}} \phi - \phi_{\text{bed}_j}\right) \\ & + q_\phi \end{aligned} \tag{2.9}$$

The first term of equation 2.9, $\lambda_\phi \phi d$, represents contaminant decay where λ is the constant decay rate. This is usually used to represent radioactive decay, but it can be used to represent any process that can be approximated as a first-order decay (Fischer et al. 1979). The decay rate is computed from the half-life, $t_{\phi_{1/2}}$, as

$$\lambda = \frac{\ln 2}{t_{\phi_{1/2}}} \tag{2.10}$$

The second term of equation 2.9, represents the exchange with all of the suspended particulate phases of the scalar ϕ (one for each sediment fraction j). $K_{d_{\phi_j}}$ is a partitioning coefficient specific to the scalar ϕ and sediment fraction j (Onishi and Thompson 1984). The value of $K_{d_{\phi_j}}$ is the ratio of particulate to dissolved contaminant when they are in equilibrium:

$$K_{d_{\phi_j}} = \frac{\phi_{\text{part}_j}}{\phi_{\text{sed}_j} \phi} \tag{2.11}$$

where ϕ_{part_j} is the volumetric concentration of particulate contaminant, ϕ_{sed_j} is the volumetric concentration of sediment fraction j, and $K_{d_{\phi_j}}$ is a partitioning coefficient specific to the scalar ϕ and sediment fraction j. The second term of equation 2.9 represents the rate at which contaminant mass is exchanged between the dissolved and particulate phases to achieve the equilibrium described by equation 2.11. The magnitude of the exchange is governed by the dissolved/particulate imbalance and the rate at which contaminant is exchanged between phases, K_{ϕ_j}, which has dimensions of time^{-1}.

The third term of equation 2.9 similarly represents the exchange of dissolved contaminant within the water column with any particulate contaminant on the bed surface. The exchange is assumed to be limited to the surface of the bed, or the mass of sediment fraction j occupying a thickness of one sediment grain width, D_{50_j}, at the top of the bed.

The final term, q_ϕ, represents any other sources. This term is used to supply contaminants to the water column from non-point sources like groundwater. Section 3.8.2 describes how this is computed.

2.3.2 Suspended Sediment Source Term

The general transport equation, equation 2.8, is used to represent the transport of sediment suspended in the water column. An arbitrary number of sediment fractions can be simulated simultaneously and are assumed to be independent of each other. The source term in equation 2.12 for sediment fraction j is the difference between erosion from and deposition to the bed:

$$S_{\text{sed}_j} = E_j - D_j \tag{2.12}$$

where S_{sed_i} has dimensions of mass per unit bed area per time. E_j is the erosion rate of sediment fraction j, given by (Partheniades 1962)

$$E_j = \begin{cases} \left(\dfrac{\tau_b}{\tau_{e_j}} - 1\right) E_{o_j}, & \text{if } \tau_b > \tau_{e_j} \\ 0, & \text{if } \tau_b \leq \tau_{e_j} \end{cases} \tag{2.13}$$

where τ_b is the bed shear computed from the hydrodynamic state (equations 2.5 and 2.6), E_{o_j} is the erodibility coefficient for sediment fraction j, and the critical erosion shear stress, τ_{e_j}, represents the shear at which erosion of sediment fraction j is initiated. The erosion rate computed using equation 2.13 is limited by the availability of sediment fraction j in the bed.

D_j is the deposition rate of sediment fraction j, given by (Krone 1962)

$$D_j = \begin{cases} \left(1 - \dfrac{\tau_b}{\tau_{d_j}}\right) w_j \phi_{\text{sed}_j}, & \text{if } \tau_b < \tau_{d_j} \\ 0, & \text{if } \tau_b \geq \tau_{d_i} \end{cases} \tag{2.14}$$

where ϕ_{sed_j} is the volumetric concentration, w_j is the particle settling velocity, and τ_{d_i} is the critical deposition shear stress for sediment fraction j.

The coefficients w_j, τ_{e_j}, τ_{d_j}, and M_j are properties specific to the sediment fraction (other properties are required as well, see Section 3.8). Their values will vary depending the sediment particle size, chemical composition of the sediment, and other local conditions. Consequently, they are determined by calibration.

2.3.3 Particulate Scalar Source Term

When equation 2.8 is used to represent the transport of the particulate phases of a contaminant, the transported quantity is the volumetric concentration of the contaminant sorbed to an individual sediment fraction, j. The source term of equation 2.8 takes the form

$$\begin{aligned} S_{\phi_{\text{part}_j}} = & -\lambda_\phi \phi_{\text{part}_j} d \\ & - \sum_{j=1}^{N_{\text{sed}}} K_{\phi_j} \left(K_{d_{\phi_j}} \phi_{\text{sed}_j} \phi - \phi_{\text{part}_j} \right) \\ & + \left(\phi_{\text{bed}_j} E_j - \frac{D_j \phi_{\text{part}_j}}{\phi_{\text{sed}_j}} \right) \end{aligned} \tag{2.15}$$

The first term of equation 2.15 represents decay, as in equation 2.9. The second term represents exchange with the dissolved phase and corresponds to the second term of equation 2.9. The third term represents the particulate mass deposited to or eroded from the bed, with the deposition (D_j) and erosion (E_j) determined as in equation 2.12.

2.3.4 Thermal Energy (Temperature) Source Term

When equation 2.8 is used to represent the transport of thermal energy, the transported quantity is the depth-averaged water temperature, T, in °C, and the source term has the form

$$S_T = \frac{\Sigma H}{\rho c_v} \tag{2.16}$$

where c_v is the specific heat of water (assumed constant at 4186 J/kg·°C) and ΣH is the net heat exchange at the water surface, W/m^2, which is represented as

$$\sum H = H_{sn} + H_a - (H_b + H_e + H_c) \tag{2.17}$$

where the units are W/m^2.

H_{sn} is the net incoming solar short-wave radiation and was computed using measured or estimated incoming shortwave solar radiation. H_{sn} is based on either measured values of incoming solar radiation, when available, or from theoretical estimates and a measurement of cloud cover. When measured radiation is available,

$$H_{sn} = H_a (1 - R_s)$$

where H_a is the measured short-wave solar radiation at the surface, W/m^2, and R_s is the albedo or reflection coefficient. The albedo is calculated by (Brown and Barnwell 1987):

$$R_s = A \left(\frac{180\alpha}{\pi} \right)^B \tag{2.18}$$

where

$$A = \begin{cases} 1.18 \text{ for } C_L < 0.1 \\ 2.20 \text{ for } 0.1 \le C_L < 0.5 \\ 0.95 \text{ for } 0.5 \le C_L < 0.9 \\ 0.35 \text{ for } C_L > 0.9 \end{cases}$$

and

$$B = \begin{cases} -0.77 \text{ for } C_L < 0.1 \\ -0.97 \text{ for } 0.1 \le C_L < 0.5 \\ -0.75 \text{ for } 0.5 \le C_L \le 0.9 \\ -0.45 \text{ for } C_L > 0.9 \end{cases}$$

where C_L is the cloudiness. The solar altitude, α, is calculated using (Gates 1980; Monteith and Unsworth 1990)

$$\sin\alpha = \sin\Phi \sin\delta + \cos\Phi \cos\delta \cos h$$

where Φ is the site latitude, δ is the declination of the sun, given by (Duffie and Beckman 1982)

$$\delta = 23.45 \frac{\pi}{180d} \sin\left(2\pi \left[\frac{284+j}{365}\right]\right)$$

and $h = (\pi/12)(t_s - 12)$. t_s is the solar time, in hours, given by

$$t_s = t_l + \frac{12}{\pi}(L_{\text{st}} - L_{\text{loc}}) + E$$

E is the equation of time, given by (Duffie and Beckman 1982)

$$E = (9.87 \sin 2B - 7.53 \cos B - 1.5 \sin B)/60$$

with $B = [2\pi(n-81)]/364$.

When measured radiation is not available, net incoming short-wave solar radiation can be estimated using (Brown and Barnwell 1987)

$$H_{sn} = H_o a_t (1 - R_s)\left(1 - 0.65 C_L^2\right)$$

in which H_o is estimated using (Duffie and Beckman 1982; Wigmosta and Perkins 1997)

$$H_o = H_{sc}\left[1 + 0.033 \cos\left(\frac{360n}{365}\right)\right] \sin\alpha$$

where H_{sc} is the solar constant (approximately 1360 W/m^2) and n is the day of the year.

The other components of equation 2.17 are computed according to Edinger et al. (1974). Net incoming atmospheric long-wave radiation is estimated as

$$H_a = 4.4 \times 10^{-8}(T_a + 273)^4 \left[C_a + 0.031\sqrt{e_a}\right] \tag{2.19}$$

where C_a is the Brunt coefficient, typically having a value of 0.65. Long-wave back-radiation was estimated as

$$H_b = \varepsilon_w \sigma^* (T + 273.15)^4$$

where T is the cross section averaged water temperature. Evaporation heat flux was computed using

$$H_e = \left(a_w + b_w W^2\right)(e_s - e_a) \tag{2.20}$$

where W is the wind speed, in m/sec, a_w and b_w are adjustable wind function coefficients, e_s is the saturation water vapor pressure at the water surface (a function of current air temperature), in mm Hg, and e_a is the actual water vapor pressure at the water surface, in mm Hg. Conduction heat flux was computed as

$$H_c = C_c\left(a_w + b_w W^2\right)(T_s - T_a) \tag{2.21}$$

where C_c is typically 0.46.

2.3.5 Total Dissolved Gas

When equation 2.8 is used to represent total dissolved gas (TDG), the source term represents the exchange of dissolved gas in the water column with the atmosphere. The source term has the form

$$S_{\mathrm{TDG}} = K_L (C_* - C) \tag{2.22}$$

where C is the volumetric concentration of air in water, mg/L, C_* is the saturation concentration of air in water at the surface, mg/L, and K_L is a surface transfer coefficient. Many air-water gas exchange formulas are available in the literature. In MASS2, K_L is a function of wind speed and given by a fit of a cubic polynomial equation to empirical data presented by O'Connor (1982, Figure 6 intermediate scale data):

$$\begin{aligned} K_L &= dW^3 + cW^2 - bW + a \\ &= -0.0045W^3 + 0.1535W^2 - 0.5026W + 0.6885 \end{aligned} \tag{2.23}$$

where K_L is in m/day and W is the wind speed in m/sec, 10 m above the water surface.

Because it is convenient to present TDG simulation results as TDG partial pressures or a fraction of the saturation partial pressure, MASS2 computes partial TDG pressures and saturations internally. Calculation of TDG pressures and saturations from a given concentration, and vice versa, is accomplished using the relationships presented in Colt (1984). The mass concentration of TDG is related to partial pressure with

$$C = \frac{(P_{\mathrm{TDG}} - P_{\mathrm{H_2O}})\,\beta_{\mathrm{air}}}{A_{\mathrm{air}}}$$

where P_{TDG} is the partial pressure of TDG, mm Hg, $P_{\mathrm{H_2O}}$ is the vapor pressure of water, mm Hg, β_{air} is the apparent Bunsen coefficient for air, L/L·atm, and A_{air} is the apparent molecular volume of air (with unit conversion), atm·L/mg·mm Hg. Air is assumed to be composed of a limited number, N, of individual gases. These are shown in Table 2.1. The apparent Bunsen coefficient for air is computed as an aggregate of the Bunsen coefficients for individual gas fractions:

$$\beta_{\mathrm{air}} = \frac{\sum_{i=1}^{N} \beta_i X_i}{\sum_{i=1}^{N} X_i}$$

where β_i is the Bunsen coefficient for gas fraction i, L/L·atm, and X_i is the mole fraction of gas i. The mole fractions used are those for atmospheric air and are shown in Table 2.1. Individual gas fraction Bunsen coefficients are computed as functions of temperature using relationships presented by Colt (1984), as is water vapor pressure, $P_{\mathrm{H_20}}$. The apparent molecular volume of air is computed as an aggregate of individual gas fractions:

$$A_{\mathrm{air}} = \frac{760}{1000} \left(\frac{\sum_{i=1}^{N} \beta_i X_i}{\sum_{i=1}^{N} K_i \beta_i X_i} \right)$$

where K_i is the ratio of molecular weight to molecular volume, g/L, for gas fraction i, the values of which are shown in Table 2.1.

Table 2.1. Gas fractions used to compute gas mass concentrations from gas pressures (Colt 1984). Mole fractions are for atmospheric air.

Gas Fraction	X_i	K_i, g/L
Nitrogen (N_2)	0.78084	1.25043
Oxygen (0_2)	0.20946	1.42903
Argon (Ar)	0.00934	1.78419
Carbon Dioxide (CO_2)	0.00032	1.97681

3.0 Numerical Methods

3.1 Computational Mesh

The computational mesh is supplied to MASS2 as a set of vertices in the physical coordinate system (Figure 3.1). From these vertices, metric coefficients (Section 2.1) are computed (using finite-differences) to transform the mesh into a rectangular grid in computational space. For convenience, mesh blocks are labeled according to the expected flow direction: the four sides are labeled as upstream, downstream, left bank, and right bank. It is also convenient, for discretization of the governing equations, to label the four sides as directions: west being upstream, east being downstream, south being the right bank, north being the left bank.

The vertices define the corners of cells. At the center of these cells, depth and transported scalar quantities are computed. Velocities are computed at the cell faces using staggered control volumes (CV) to avoid unrealistic solutions to the coupled continuity-momentum equations as discussed by Patankar (1980). Bottom elevation is supplied with each vertex location. This defines the bathymetry for MASS2. When bottom elevations are required at other locations (the cell center, e.g.), they are interpolated from the vertex elevations as necessary.

Mesh blocks can be connected to other blocks. These blocks abut each other and must line up such that an integral number of cells in one block abut a single cell in the other. Connected blocks share necessary information through ghost cells. When the model grid is first read by the model, a layer of ghost cells is created on all sides of each block. If the ghost cell corresponds to a connected block, the ghost cell size and shape is based on the cells in the connected block. If the ghost cell does not correspond to a connecting cell, the cell size and shape is extrapolated from the block interior. Using this strategy allows grid metric coefficients to be correctly computed near block edges, particularly for the staggered velocity CVs.

3.2 Discrete Forms of Governing Equations

The governing equations in the model are discretized using the finite-volume methods described by Patankar (1980). The momentum and scalar transport equations are discretized using similar methods. The discretized scalar transport equation is presented first in Section 3.2.1. Following that derivation, the specific issues related to discretizing the momentum equations and the depth-velocity coupling are presented in Section 3.2.2.

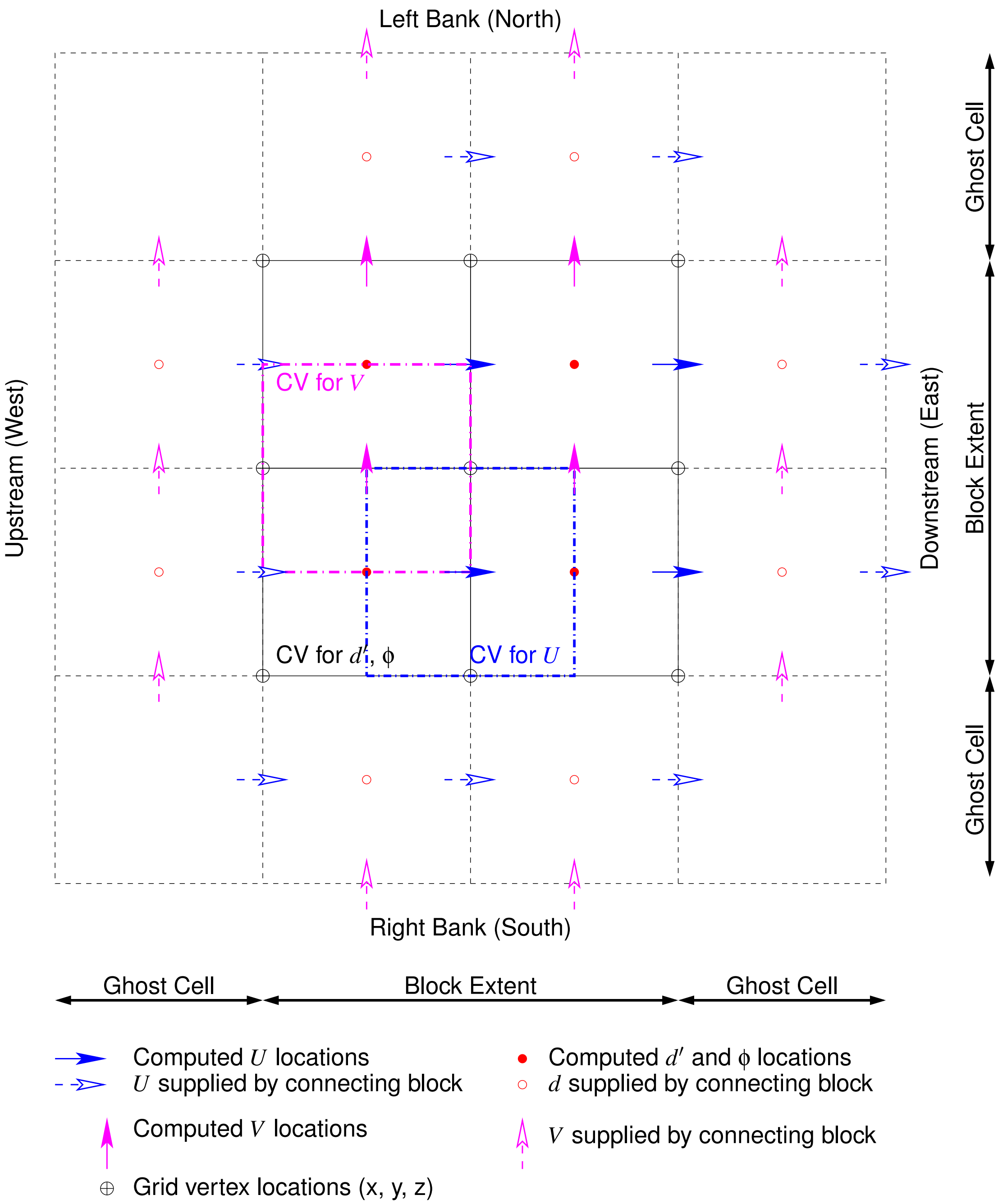
Left Bank (North)
Upstream (West)
Downstream (East)
Right Bank (South)
Ghost Cell
Block Extent
Ghost Cell
CV for V
CV for d', ϕ
CV for U
Ghost Cell
Block Extent
Ghost Cell
Computed U locations
U supplied by connecting block
Computed V locations
Grid vertex locations (x, y, z)
Computed d′ and ϕ locations
d supplied by connecting block
V supplied by connecting block

Figure 3.1. Layout of the MASS2 computational mesh for a single block.

3.2.1 Discretized Form of the General Scalar Transport Equation

The general scalar transport equation (2.8) can be rearranged into the form

$$h_1 h_2 \frac{\partial (d\phi)}{\partial t} + \frac{\partial J_\xi}{\partial \xi} + \frac{\partial J_\eta}{\partial \eta} = h_1 h_2 S_\phi \tag{3.1}$$

where the total flux in each direction is

$$J_\xi = (h_2 d U \phi) - h_2 \frac{\varepsilon_1}{h_1} d \frac{\partial \phi}{\partial \xi} \tag{3.2}$$

$$J_\eta = (h_1 d V \phi) - h_1 \frac{\varepsilon_2}{h_2} d \frac{\partial \phi}{\partial \eta} \tag{3.3}$$

Equation 3.1 can then be integrated over the control volume to obtain

$$h_1 h_2 \frac{\left(d_P \phi_P - d_P^0 \phi_P^0\right)}{\Delta t} + J_e - J_w + J_n - J_s = h_1 h_2 (S_C + S_P \phi_P) \tag{3.4}$$

where the time derivative is formulated using the implicit Euler scheme and d_P^0 and ϕ_P^0 are evaluated at the previous time step. The flux terms (J_e, etc) are computed at the east, west, north, and south CV faces. The source term is linearized into a constant part (S_C) and a part the depends on ϕ (S_P).

The fluid continuity or mass conservation (equation 2.1) can also be integrated over a CV to yield the following

$$h_1 h_2 \frac{(d_P - d_P^0)}{\Delta t} + F_e - F_w + F_n - F_s = 0 \tag{3.5}$$

where the fluid mass flux (F_e, etc) through each face of the CV is

$$F_e = (h_2 U d)_e \tag{3.6}$$

$$F_w = (h_2 U d)_w \tag{3.7}$$

$$F_n = (h_1 V d)_n \tag{3.8}$$

$$F_s = (h_1 V d)_s \tag{3.9}$$

As recommended by Patankar (1980), the final form of the discrete general scalar transport equation can by multiplying equation 3.5 by ϕ_P and then subtracting that from equation 3.4 to obtain

$$\begin{aligned} h_1 h_2 \frac{\left(\phi_P d_P^0 - \phi_P^0 d_P^0\right)}{\Delta t} &+ (J_e - F_e \phi_P) - (J_w - F_w \phi_P) \\ &+ (J_n - F_n \phi_P) - (J_s - F_s \phi_P) = h_1 h_2 (S_C + S_P \phi_P) \end{aligned} \tag{3.10}$$

Each of the total flux terms can be represented using the values in the center of each CV in the form

$$
\begin{aligned}
J_e - F_e\phi_P &= a_E(\phi_P - \phi_E) && (3.11)\\
J_w - F_w\phi_P &= a_W(\phi_W - \phi_P) && (3.12)\\
J_n - F_n\phi_P &= a_N(\phi_P - \phi_N) && (3.13)\\
J_s - F_s\phi_P &= a_S(\phi_S - \phi_P) && (3.14)
\end{aligned}
$$

where the coefficients in these and the remaining flux terms are

$$
\begin{aligned}
a_E &= D_eA(|P_e|) + \max[-F_e, 0] && (3.15)\\
a_W &= D_wA(|P_w|) + \max[F_w, 0] && (3.16)\\
a_N &= D_nA(|P_n|) + \max[-F_n, 0] && (3.17)\\
a_S &= D_sA(|P_s|) + \max[F_s, 0] && (3.18)
\end{aligned}
$$

and the effective diffusion coefficient (D) and Peclet number (P) are

$$
\begin{aligned}
D_e &= \left(\varepsilon_1 d\frac{h_2}{h_1}\right)_e && (3.19)\\
D_w &= \left(\varepsilon_1 d\frac{h_2}{h_1}\right)_w && (3.20)\\
D_n &= \left(\varepsilon_2 d\frac{h_1}{h_2}\right)_n && (3.21)\\
D_s &= \left(\varepsilon_2 d\frac{h_1}{h_2}\right)_s && (3.22)\\
P_e &= \frac{(h_2Ud)_e}{D_e} && (3.23)\\
P_w &= \frac{(h_2Ud)_w}{D_w} && (3.24)\\
P_n &= \frac{(h_1Vd)_n}{D_n} && (3.25)\\
P_s &= \frac{(h_1Vd)_s}{D_s} && (3.26)
\end{aligned}
$$

These coefficients result from discretizing the diffusive flux using the central-difference approximation and where the advective flux term can be discretized using various schemes which can be selected by various choices for the function $A(|P|)$. Some common choices for $A(|P|)$ are listed in Table 3.1.

The final discretized form of equation 2.8 is then

$$
\begin{aligned}
a_{\mathrm{P}}\phi_{\mathrm{P}} &= a_{\mathrm{W}}\phi_{\mathrm{W}} + a_{\mathrm{E}}\phi_{\mathrm{E}} + a_{\mathrm{S}}\phi_{\mathrm{S}} + a_{\mathrm{N}}\phi_{\mathrm{N}} + b\\
a_{\mathrm{P}} &= a_{\mathrm{W}} + a_{\mathrm{E}} + a_{\mathrm{S}} + a_{\mathrm{N}} + a_{\mathrm{P}}^0 - S_{\mathrm{P}}h_1h_2\\
a_{\mathrm{P}}^0 &= \frac{h_1h_2d_P^0}{\Delta t}\\
b &= S_Ch_1h_2 + a_P^0\phi_P^0
\end{aligned}
\qquad (3.27)
$$

Table 3.1. Function $A(|P|)$ for different advection schemes

Scheme	$A(\|P\|)$
Upwind	1
Hybrid	$\max[0, 1-0.5\|P\|]$
Power law	$\max[0, 1-0.1\|P\|^5]$

for each control volume (CV) P (Figure 3.1), where the subscripts W, E, S, and N refer to the CVs neighboring P on the west, east, south, and north sides. S_P and S_C refer to the ϕ-dependent and constant parts of the source term, respectively.

The hybrid scheme (Patankar 1980) is used for the adjective term in the solution of scalar transport equations in MASS2. This allows for a zero diffusive flux, which is necessary when internal "dead" zones, or dry cells, are simulated.

Note that the orthogonal curvilinear form of the discretization equations presented reduce to the typical Cartesian form if the coordinate transformation is considered to be from a nonuniform Cartesian grid to the uniform computational domain and the metric coefficients (h_1, h_2) are replaced by $(\Delta x, \Delta y)$, respectively.

Equation 3.27 is implicit in space and time. The assembly of these equations for each numerical CV results in a system of linear equations that are solved using a line-by-line tridiagonal matrix algorithm (TDMA) (Versteeg and Malalasekera 1995). Others methods are optional using the Aztec (Tuminaro et al. 1999) library and the Portable, Extensible Toolkit for Scientific Computation (PETSc) Balay et al. (1997, 2002). These are usually not used because the TDMA algorithm performs efficiently for most applications.

3.2.2 Discretized Form of the Momentum Equations

The momentum equations (2.2 and 2.3) can be put in the same form as the scalar transport equation (2.8). The additional terms arising from the coordinate transformation are grouped into the source term. These source terms, which include the depth gradient, bottom elevation gradient, and bed resistance are evaluated using finite-difference expressions in the computational grid.

As in Patankar (1980), a staggered numerical grid is employed to oid the computation of unrealistic depth and velocity fields. Consequently, the momentum equations are solved at different locations and CVs than transported scalars (Figure 3.1).

The power-law scheme (Patankar 1980) (see Table 3.1) is used for the advection terms in the momentum equations. It should be noted that the power-law scheme reduces to first-order accuracy for high values of the grid Peclet number (advection-dominated cases) and therefore introduces artificial diffusion when the computational grid lines and streamlines are not aligned. In the majority of applications, artificial diffusion will be minimal if the computational mesh lines and streamlines are approximately aligned. Higher-order schemes can be used to minimize artificial diffusion but this increased accuracy comes at the price of additional computational effort that Ye and McCorquodale (1997) estimate to be 40 to 70% more than the power-law scheme. Future development plans (see Chapter 5) include adding a monotonic, higher-order advection scheme to MASS2.

Experience has shown that the handling of the bed shear (resistance) term (equations 2.5 and 2.6) of the momentum equations is very important to the success of the overall hydrodynamic solution in MASS2. In the momentum equations for U, for example, the contribution bed shear force to the source term estimated by

$$S = -A_{\mathrm{P}} U_{\mathrm{P}} \overline{V}_{\mathrm{P}}$$

where $\overline{V}_{\mathrm{P}}$ is the velocity magnitude at the U CV center, given by $\sqrt{U_{\mathrm{P}}^2 + V_{\mathrm{P}}^2}$, U_{P} and V_{P} are the longitudinal and lateral velocity at the U CV center, and C_{P} is the collected constants (with respect to U) from equation 2.5. To linearize this term, it is separated into a constant and U dependent part (Patankar 1980):

$$S = S_{\mathrm{C}} + S_{\mathrm{P}} U_{\mathrm{P}}$$

The previous estimate of U_{P}, U_{P}^*, is used to evaluate the velocity magnitude using the previous estimate of U_{P}:

$$S = -A_{\mathrm{P}} U_{\mathrm{P}} \overline{V}_{\mathrm{P}}^*$$

so that

$$\begin{aligned} S_{\mathrm{C}} &= 0 \\ S_{\mathrm{P}} &= -A_{\mathrm{P}} \overline{V}_{\mathrm{P}}^* \end{aligned}$$

3.2.3 Velocity-Depth Coupling

The coupling of the momentum and mass conservation equations is achieved using a variation of Patankar (1980) SIMPLE algorithm extended to depth-averaged flows by Zhou (1995). Zhou's method has been extended here to orthogonal curvilinear coordinates in the present study. In the method, equation 2.1 is used to develop an equation of the form of 3.27 and solved for a depth correction, d' (in lieu of the pressure correction in the original SIMPLE algorithm). The solution to the depth correction equation is used to correct the velocities from the solution of the momentum equations. A portion of the depth correction is used to adjust depth.

Given a water depth distribution (d^*) at the current iteration, the depth-averaged velocities (U^*, V^*) can be computed from the discretized momentum equations:

$$\begin{aligned} a_P U_P^* &= \sum a_{nb} U_{nb}^* - \frac{g h_{2P}}{2} \left[d_e^{*2} - d_w^{*2} \right] - \frac{g h_{2P}}{2} \left[d_e^* + d_w^* \right] \left[z_e - z_w \right] + b_U && (3.28) \\ a_P V_P^* &= \sum a_{nb} V_{nb}^* - \frac{g h_{1P}}{2} \left[d_n^{*2} - d_s^{*2} \right] - \frac{g h_{1P}}{2} \left[d_n^* + d_s^* \right] \left[z_n - z_s \right] + b_V && (3.29) \end{aligned}$$

Recall that the use of a staggered grid means that the CVs for each velocity component are different and that the locations of the control volume faces (east, west, etc) and central point are relative to that particular CV.

Although the iterative solution of equations 3.28 and 3.29 will yield the velocity field corresponding to the prescribed depth field that velocity field may fail to satisfy the continuity equation 2.1. A method is needed to iteratively correct the velocity and depth fields so that the continuity and momentum equations are both satisfied. This method is the SIMPLE algorithm adapted to depth-averaged flows solved on an orthogonal curvilinear grid.

The correct depth and velocity field is composed of the value at the current iteration plus a correction term:

$$\begin{aligned} d &= d^* + d' \\ U &= U^* + U' \\ V &= V^* + V' \end{aligned}$$

where (d^*, U^*, V^*) are the current values and (d', U', V') are the correction terms. A discrete equation for the velocity corrections can be derived by subtracting the current iteration value from the final velocity $(U' = U - U^*)$:

$$a_P U'_P = \sum a_{nb} U'_{nb} - \frac{g h_{2P}}{2}\left[d_e^2 - d_w^2 + d_w^{*2} - d_e^{*2}\right] - \frac{g h_{2P}}{2}\left[d'_e + d'_w\right]\left[z_e - z_w\right] \tag{3.30}$$

This equation can be expanded to obtain

$$\begin{aligned} a_P U'_P = \sum a_{nb} U'_{nb} &- \frac{g h_{2P}}{2}\left[d_e^* + d_w^*\right]\left[d'_e - d'_w\right] - \frac{g h_{2P}}{2}\left[d'_e + d'_w\right]\left[d_e^* - d_w^*\right] \\ &- \frac{g h_{2P}}{2}\left[d_e'^2 - d_w'^2\right] - \frac{g h_{2P}}{2}\left[d'_e + d'_w\right]\left[z_e - z_w\right] \end{aligned} \tag{3.31}$$

Following Patankar (1980) and Zhou (1995) the first and last three terms of equation 3.31 are dropped which yields an equation for the velocity correction:

$$U'_P = -\frac{g h_{2P}}{2}\frac{\left[d_e^* + d_w^*\right]}{a_P}\left[d'_e - d'_w\right] \tag{3.32}$$

A similar equation for the other velocity correction (V'_P) can be derived using the same method. The updated velocity can now be expressed as

$$U_P = U_P^* - \frac{g h_{2P}}{2}\frac{\left[d_e^* + d_w^*\right]}{a_P}\left[d'_e - d'_w\right] \tag{3.33}$$

This equation for the U velocity and the corresponding equation for the V velocity can be substituted into the discrete continuity equation 3.5 to arrive at a discrete equation for the depth correction:

$$c_P d'_P = c_E d'_E + c_W d'_W + c_N d'_N + c_S d'_S + M^* \tag{3.34}$$

where

$$
\begin{aligned}
c_P &= c_E + c_W + c_N + c_S + c_P^0 \\
c_P^0 &= \frac{h_{1P} h_{2P}}{\Delta t} \\
c_E &= (h_2 d)_e \left[\frac{g h_{2P}}{2} \frac{[d_e^* + d_w^*]}{a_{P_U}} \right]_{U_e} \\
c_W &= (h_2 d)_w \left[\frac{g h_{2P}}{2} \frac{[d_e^* + d_w^*]}{a_{P_U}} \right]_{U_w} \\
c_N &= (h_1 d)_n \left[\frac{g h_{1P}}{2} \frac{[d_n^* + d_s^*]}{a_{P_V}} \right]_{V_n} \\
c_S &= (h_1 d)_s \left[\frac{g h_{1P}}{2} \frac{[d_n^* + d_s^*]}{a_{P_V}} \right]_{V_s} \\
M^* &= c_P^0 (d_P^0 - d_P^*) + (h_2 d)_w U_w^* - (h_2 d)_e U_e^* + (h_1 d)_s V_s^* - (h_1 d)_n V_n^*
\end{aligned}
$$

Note that the CV for the depth correction equation is the same as that used for scalar variables.The bracketed terms in the coefficients c_E, etc should be calculated and stored when at the time when the subscripted velocities ($[\cdots]_{U_e}$, etc) are computed in their respective CVs. The term M^* is the so-called mass source since it is the negative of the discrete continuity equation 3.5. When the mass source is driven to zero then the depth correction will also be zero. At this time both the continuity and momentum equations are satisfied.

The depth correction equation is solved using the same iterative solution methods as used for the general scalar transport equation in Section 3.2.1.

3.3 Solution Procedure

MASS2 begins execution by reading the configuration and allocating the memory necessary to store variables for the problem. The mesh is then read, appropriate ghost cells created, and mesh metric coefficients computed. Boundary and initial conditions are read and set.

The overall procedure for simulation is essentially a time loop (Figure 3.2). During a time step, execution depends on the operational mode selected. If active, hydrodynamics (Section 3.3.1) are solved first. The transport solution (Section 3.3.2) is then performed. After solution is complete, the "old" values of variables are updated with the new, and optionally, output is accumulated to average conditions over the output interval rather than instantaneous values.

3.3.1 Hydrodynamics

Nonlinearity and coupling of the momentum (Section 3.2.2) and depth correction (Section 3.2.3) equations are handled through an iterative solution procedure (Figure 3.3). In a single iteration of

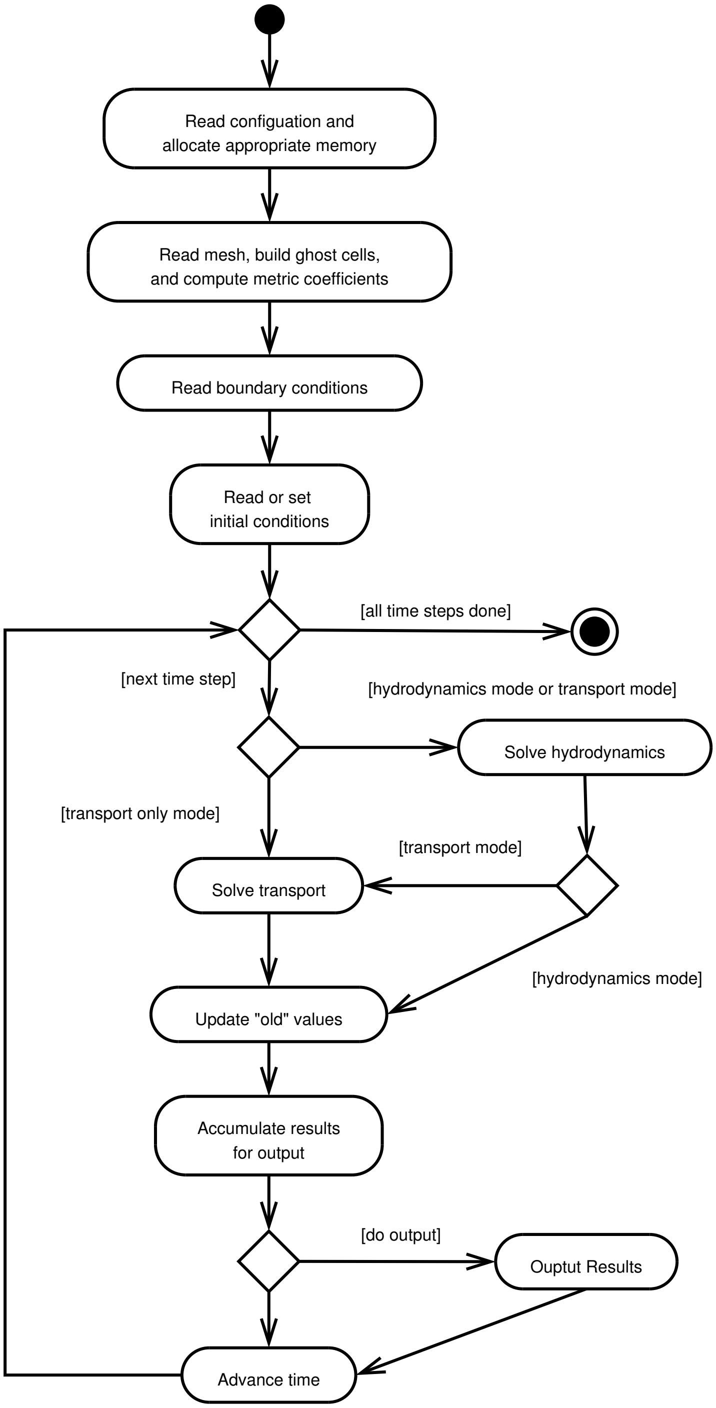
Read configuation and
allocate appropriate memory
Read mesh, build ghost cells,
and compute metric coefficients
Read boundary conditions
Read or set
initial conditions
[all time steps done]
[next time step]
[hydrodynamics mode or transport mode]
Solve hydrodynamics
[transport only mode]
[transport mode]
Solve transport
[hydrodynamics mode]
Update "old" values
Accumulate results
for output
[do output]
Ouptut Results
Advance time

Figure 3.2. Solution algorithm flow chart.

the hydrodynamic solution, each block is solved independently, assuming conditions in the surrounding blocks are constant. The solution of a single block proceeds as follows

1. The necessary values (U, V, d) from neighboring blocks are copied into ghost cells (Section 3.6), *or* specified boundary conditions are assigned (Section 3.5).

2. Coefficients for the discretized equation for U-momentum are assembled, and the resulting system of equations is solved.

3. Coefficients for the discretized equation for V-momentum are assembled, and the resulting system of equations solved.

4. Coefficients for the discretized equation for depth correction (d') are assembled and the system of equations solved.

5. The computed velocity components are adjusted using the computed depth correction according to equation 3.33.

6. The depth field is adjusted using only a portion of the depth correction:

   $$d = d^* + \alpha_d d'$$

   where d is the new depth, d^* is the previous estimate, and α_d is an under-relaxation factor, between 0 and 1. Typically, α_d less than 0.4 is necessary.

7. If wetting and drying is enabled, the wet/dry state of each cell is checked and appropriate adjustments made (Section 3.7).

Once all blocks are processed, the mass source error (Patankar 1980) of the domain is computed as the maximum of the individual block mass source errors. Block mass source error is the maximum cell mass imbalance computed in the solution of the depth correction equation. If the computed mass source error is less than the user-specified value, the hydrodynamic solution is complete. Otherwise, further iterations are performed until the mass source error is reduced or the user-specified maximum number of iterations is exceeded.

3.3.2 Scalar Transport

Like the hydrodynamic solution, the transport solution procedure is iterative in nature (Figure 3.4). A constant, user-specified number of iterations is performed in which each simulated scalar quantity is solved. The iterative scheme is used to couple scalar quantities with interdependencies (e.g., temperature and TDG, or particulate and dissolved phases of the same contaminant) and resolve block connections. All transported scalar source terms (Section 2.3) are evaluated using the previous estimate (i.e., explicit). Contribution of non-point sources is discussed in Section 3.8.2.

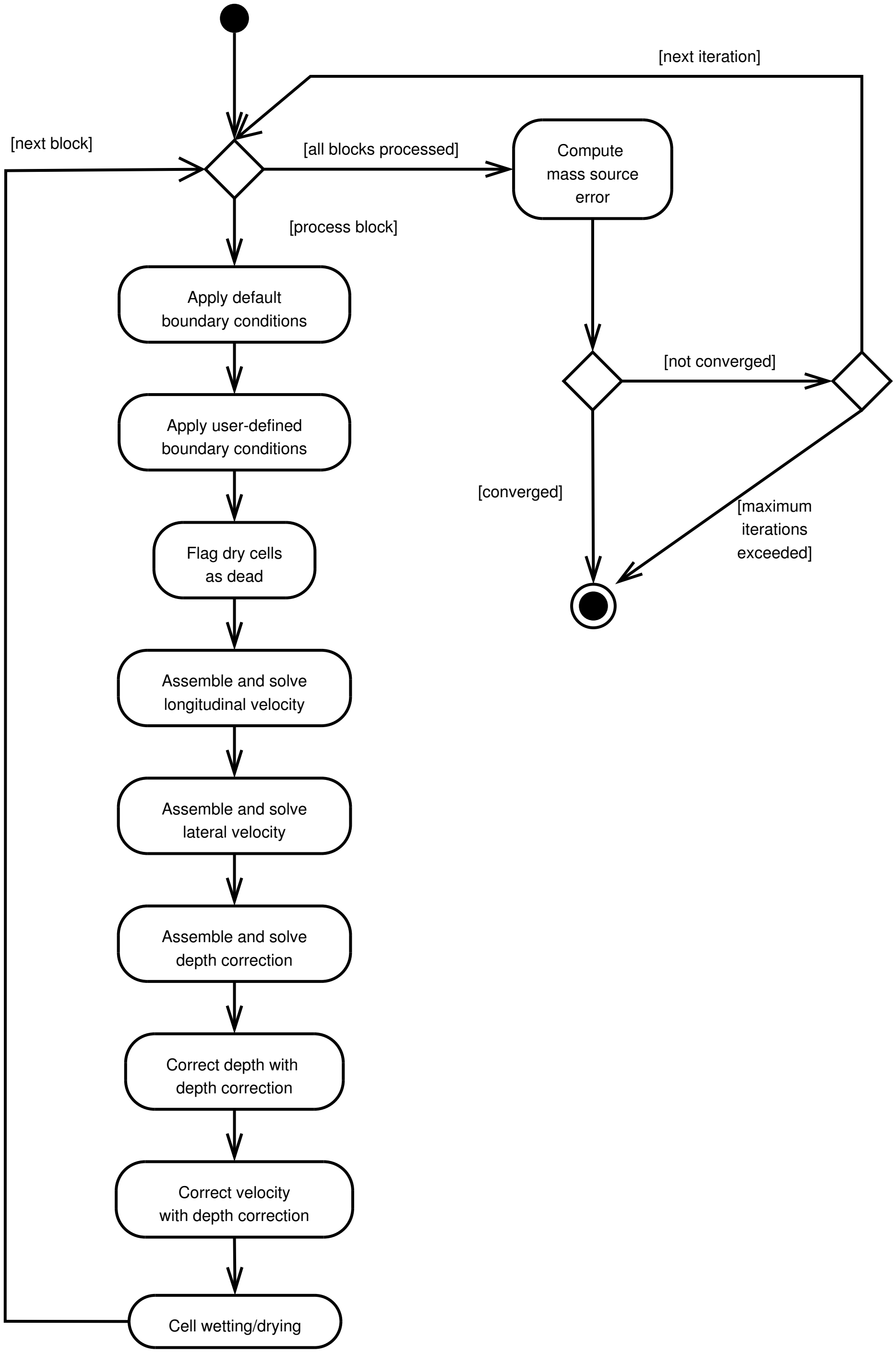
[next iteration]
[next block]
[all blocks processed]
Compute mass source error
[process block]
Apply default boundary conditions
[not converged]
Apply user-defined boundary conditions
[converged]
[maximum iterations exceeded]
Flag dry cells as dead
Assemble and solve longitudinal velocity
Assemble and solve lateral velocity
Assemble and solve depth correction
Correct depth with depth correction
Correct velocity with depth correction
Cell wetting/drying

Figure 3.3. Hydrodynamic solution algorithm flow chart.

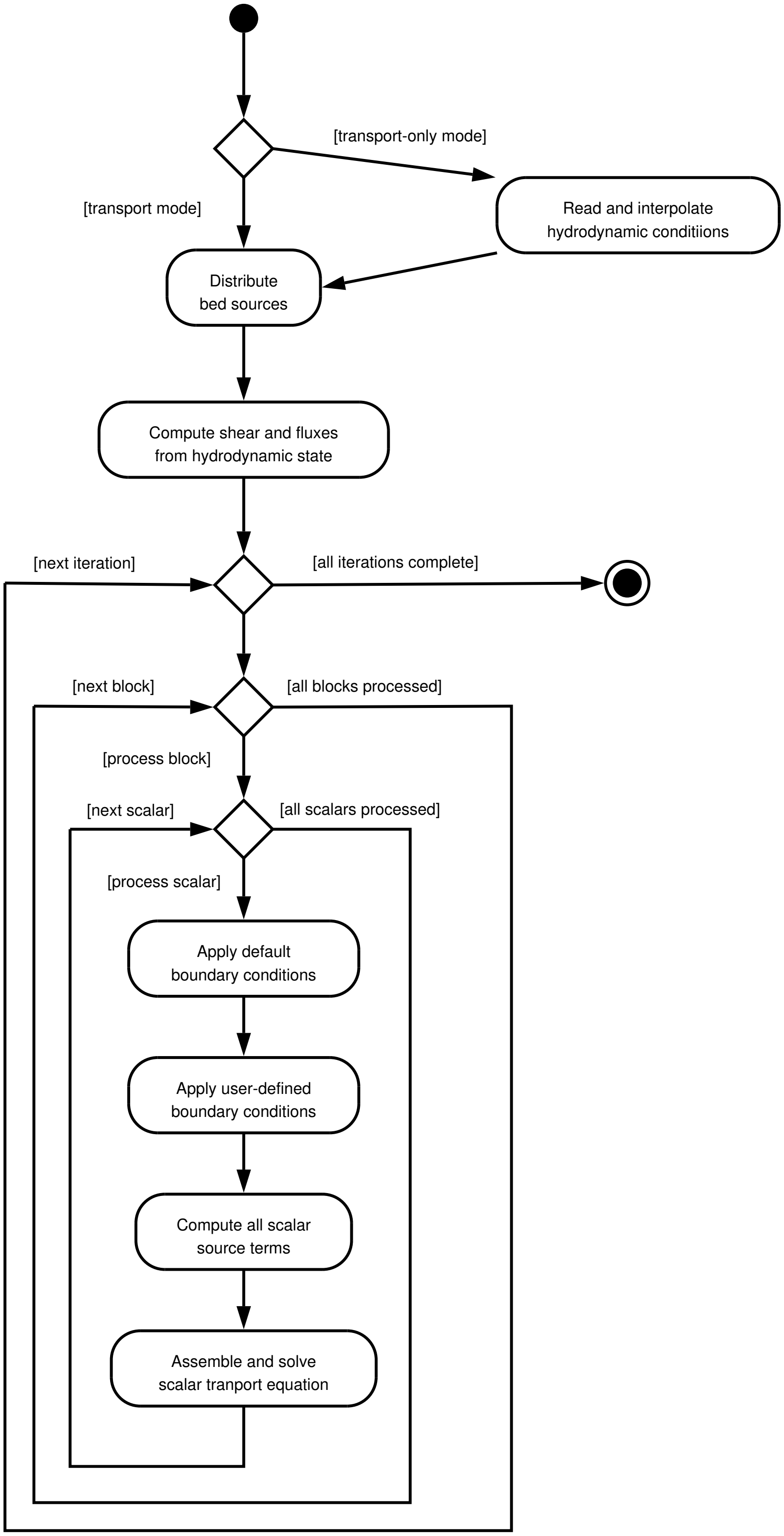
[transport-only mode]
[transport mode]
Read and interpolate hydrodynamic conditiions
Distribute bed sources
Compute shear and fluxes from hydrodynamic state
[next iteration]
[all iterations complete]
[next block]
[all blocks processed]
[process block]
[next scalar]
[all scalars processed]
[process scalar]
Apply default boundary conditions
Apply user-defined boundary conditions
Compute all scalar source terms
Assemble and solve scalar tranport equation

Figure 3.4. Scalar transport solution algorithm flow chart.

3.4 Initial Conditions

To numerically solve the system of governing equations, initial conditions must be supplied for hydrodynamics and each transported scalar. Initial conditions for each dependent variable (velocity, depth, and concentration) are assigned at the start of each simulation either as approximate values or using the results from a previous simulation (i.e., hot-start file).

Initial hydrodynamic conditions can be set using an initial water surface profile developed externally. If velocity is not supplied with the profile, it is approximated based on the local water surface slope. In some cases, this can aid model startup, particularly in applications with steep (but still subcritical) slopes. Flow from the block upstream to the downstream end is assumed. Lateral velocity (V) is assumed zero everywhere within the block. It is also assumed that the longitudinal slope of the water surface represents the energy slope (S_f) so the longitudinal velocity is estimated with Manning's equation as

$$U^* = \frac{C_o}{n} d^{2/3} S_f^{1/2}$$

where d is the average depth in the U control volume.

Initial transported scalar conditions must be set prior to solution. MASS2 can either set these to a constant value or initialize them from a previous simulation.

3.5 Boundary Conditions

The discretized form of the governing equations describes the velocity or scalar concentration at a cell center (the cell varying with the equation). Most boundary conditions are applied at the block boundary. Figure 3.5 shows the ϕ, U, and V computational cells near open block boundaries. The cells shown have the same index and are the limit of computed cells in the block. Boundary conditions are applied at block boundaries by manipulating the discretized transport equation (equation 3.27) in the manner of Norris (2000). Essentially, two boundary conditions are considered.

The first condition is assigning a given value at the boundary (Dirichlet). If, for example, $\phi = \phi_o$ is required at the west boundary, then

$$\phi_w = \phi_o \approx \frac{(\phi_\mathrm{P} + \phi_\mathrm{W})}{2} \implies \phi_\mathrm{W} = 2\phi_o - \phi_\mathrm{P}$$

where ϕ_w is the value of ϕ at the west face of the cell and P designates the central control volume. Substituting this into equation 3.27 yields

$$\begin{aligned} a_\mathrm{P}\phi_\mathrm{P} &= a_\mathrm{W}(2\phi_o - \phi_\mathrm{P}) + a_\mathrm{E}\phi_\mathrm{E} + a_\mathrm{S}\phi_\mathrm{S} + a_\mathrm{N}\phi_\mathrm{N} + S \\ (a_\mathrm{P} + a_\mathrm{W})\phi_\mathrm{P} &= a_\mathrm{E}\phi_\mathrm{E} + a_\mathrm{S}\phi_\mathrm{S} + a_\mathrm{N}\phi_\mathrm{N} + (S + 2a_\mathrm{W}\phi_o) \end{aligned}$$

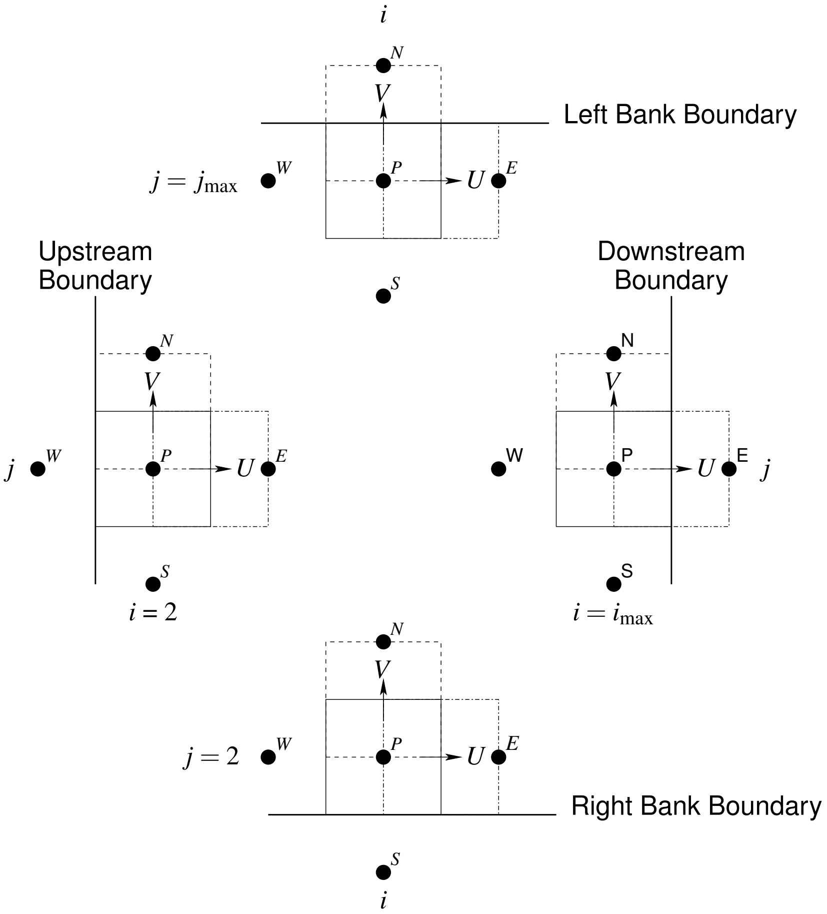
i
N
V
Left Bank Boundary
j = jmax
W
P
U
E
Upstream Boundary
Downstream Boundary
S
N
V
j
W
P
U
E
S
i = 2
N
V
W
P
U
E
j
S
i = imax
N
V
j = 2
W
P
U
E
Right Bank Boundary
S
i

Figure 3.5. Cells computed near an open block boundary. The ϕ, u, and v cells shown all have the same indices and represent the solution limits for a single block.

The Dirichlet boundary condition is then applied by adjusting some of the coefficients in the cell equation after its assembly:

$$\begin{aligned} a_P &= a_P + a_W \\ S_C &= S_C + 2a_W\phi_o \\ a_W &= 0 \end{aligned}$$

The second boundary condition is assigning a constant gradient condition at the boundary (Neumann). For example, if the gradient normal to the west face is required to be zero:

$$\frac{\partial\phi}{\partial x} \approx \frac{\phi_P - \phi_W}{\delta x} = 0 \implies \phi_P = \phi_W$$

Substituting this into equation 3.27 yields

$$\begin{aligned} a_{\mathrm{P}}\phi_{\mathrm{P}} &= a_{\mathrm{W}}\phi_{\mathrm{P}} + a_{\mathrm{E}}\phi_{\mathrm{E}} + a_{\mathrm{S}}\phi_{\mathrm{S}} + a_{\mathrm{N}}\phi_{\mathrm{N}} + S \\ \left(a_{\mathrm{P}} - a_{\mathrm{W}}\right)\phi_{\mathrm{P}} &= a_{\mathrm{E}}\phi_{\mathrm{E}} + a_{\mathrm{S}}\phi_{\mathrm{S}} + a_{\mathrm{N}}\phi_{\mathrm{N}} + S \end{aligned}$$

So, to apply the Neumann condition, coefficients of the cell equation are adjusted as follows:

$$\begin{aligned} a_{\mathrm{P}} &= a_{\mathrm{P}} - a_{\mathrm{W}} \\ a_{\mathrm{W}} &= 0 \end{aligned}$$

Because of the staggered grid scheme used in MASS2, some special consideration needs to be given boundary conditions for the momentum equations. Note in Figure 3.5 that U on the upstream (west) boundary and V on the right bank (south) boundary are not computed but must be specified. Manipulation of the cell equation, as described above, is not necessary because those locations are not part of the solution. This limits the kind of boundary condition that may be applied at those boundaries to velocity.

Velocity boundary conditions on the downstream (east) and left bank (north) sides must be handled differently. If, for example, a velocity u_o is to be applied at east side of the block, the U equation needs to be manipulated to produce that result: $U_{\mathrm{P}} = u_o$. This is done by source term manipulation (Patankar 1980). In the discretized equation, the source term S is represented as the sum of a constant part and a cell dependent part:

$$S = S_{\mathrm{C}} + S_{\mathrm{P}}U_{\mathrm{P}}$$

where U_{P} is U at the next time step (the value being solved for). To force the solution to U_{P} to the desired value (in this case u_o), a value, $K_{\mathrm{big}}U_{\mathrm{P}}$ is added to both sides of the cell equation, where K_{big} is a constant. On the constant side of the cell equation, U_{P} is set to the desired value, u_o, so

$$\begin{aligned} S &= S + K_{\mathrm{big}}u_o \\ a_{\mathrm{P}} &= a_{\mathrm{P}} + K_{\mathrm{big}} \end{aligned}$$

If K_{big} is large enough to make the other terms of the cell equation inconsequential, the solution will become

$$K_{\mathrm{big}}U_{\mathrm{P}} \approx K_{\mathrm{big}}u_o \Longrightarrow U_{\mathrm{P}} \approx u_o$$

This source term manipulation is also used to define special boundary conditions internal to the mesh block. MASS2 allows two kinds of internal boundaries: walls and dead zones. Walls block longitudinal or lateral flow by forcing the longitudinal or lateral velocity (U or V) to zero along a line of U or V CVs. These can be used to represent narrow dikes or walls that are not over-topped. Dead zones remove entire scalar cells from the simulation by forcing U velocity on the west and east faces to zero, V velocity on the south and north faces to zero, and the depth correction, d, within the cell to zero. This eliminates any change in the cell. For scalar transport, dead zone cells are essentially removed from the solution. This is done by forcing the advective and diffusive fluxes in and out of the cell to zero. The advective flux is zero because all velocities in and out of the cell have been forced to zero. To eliminate diffusive flux, the diffusivity must be set to zero. Dead zones can be used to represent small islands or other obstructions.

3.6 Mesh Block Connections

At the beginning of each hydrodynamic iteration (Section 3.3.1), the state (velocity components, water surface elevation, and scalar quantities) of the block are set in the ghost cells using the state of the neighboring block. Assembly and solution of the block then proceeds using the state of the ghost cells as though they were part of the block. From the point of view of one block, any information transferred from connected blocks is considered constant (similar to a boundary condition) during the calculations performed in a single iteration.

A special case of block connection is when the cells of the abutting blocks line up with a one-to-one correspondence. In this case, ghost cells are created with the same size and shape as the cells in the neighboring blocks. At the beginning of the iteration, the current state of the neighboring cells is simply copied into the ghost cells.

The more general block connection is when the "fine" grid block has several cells abutting a single cell in the "coarse" grid block, such as the case shown in Figure 3.6. In this case, each cell in the coarse block abuts three cells in the fine block. The size and shape of the ghost cells in the coarse grid are that of three of the neighboring fine cells grouped together. Conversely, each fine block ghost cell overlaps 1/3 of the neighboring coarse cell. In this situation, ghost cell state variables cannot be directly copied from the neighboring block.

The ghost cell value of water surface elevation any transported scalar quantity is obtained by interpolating the value from the neighboring block at the ghost cell center using a small group of neighboring cells. This interpolation is done by inverse distance weighting:

$$\phi_g = \frac{\sum_{i=1}^{N} \frac{\phi_i}{r_i}}{\sum_{i=1}^{N} \frac{1}{r_i}}$$

where ϕ_g is the value of ϕ to be placed in the ghost cell, ϕ_i is the value of ϕ in the i^{th} of N cells in the neighboring block near the center of the ghost cell, and r_i is the distance from the center of the i^{th} cell to the ghost cell center.

Velocity components are handled in a different manner because of their staggered locations. In the coarse block, the velocity component parallel to the block face (V in the example of Figure 3.6) corresponds directly to the velocity component in the fine block and can be simply be copied into the ghost cell. In the fine block, however, only some of the ghost cell values can be copied directly. The other locations fall within the neighboring coarse cell, and their values are linearly interpolated between the two values at the coarse cell sides. When setting the ghost cell value of the velocity component that crosses the block boundary (U in the case shown in Figure 3.6), it is more important to equate the fluxes across the boundary than it is to equate the velocities (Shyy et al. 1997; Thakur et al. 1997). Therefore, ghost cell velocity is computed from the flux crossing the face the neighboring block. The flux across the boundary of the coarse cell is

$$F_c = U_c A_c$$

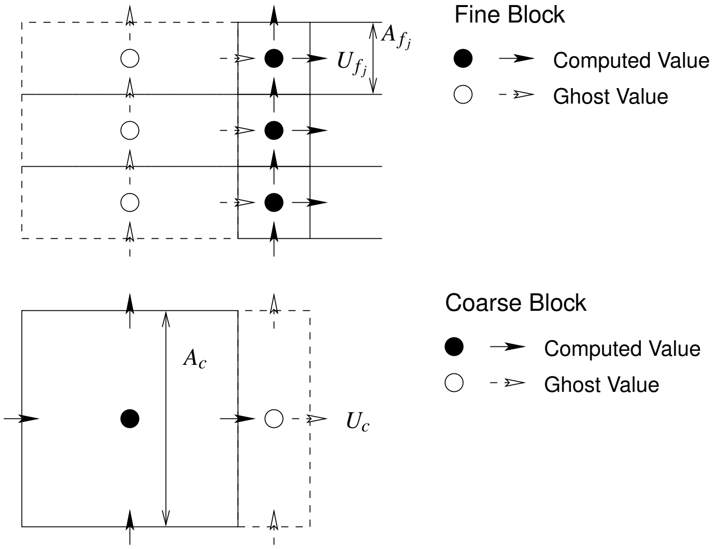

Figure 3.6. Example computational mesh block interface.

where A_c is the flow area at the coarse cell boundary. Conversely, the flux through the faces of the corresponding fine cells is

$$F_f = \sum_j U_{f_j} A f_j$$

The velocity component in the coarse ghost cell is set using the flux from the fine cells:

$$U_c = \frac{F_f}{A_c}$$

Similarly, the velocity component in the fine ghost cells is set using the flux from the coarse cell:

$$U_{f_i} = \frac{A f_i}{\sum_j A f_j} F_c$$

3.7 Wetting and Drying

Wetting and drying in MASS2 relies on a manipulation of the source term in the discretized momentum (Section 3.2.2) and depth correction (Section 3.2.3) equations to drive the solution in individual dry cells to an appropriate state. A cell is considered dry if the depth falls below a specified depth, d_{dry}. When a cell is dry, source term manipulation is used to drive the hydrodynamic solution of that cell so that the cell depth does not change (i.e., force d' to zero), and there is no flux in or out of the cell (force both U and V to zero at the cell boundaries). This is the same manner in which dead zones, discussed in Section 3.5, are handled. A dry cell remains dry until certain conditions are met such that it is allowed to rewet:

1. At least one of the cell's *wet* neighbor cells (S, N, W, E) must have a higher water surface elevation(a) than the cell.

(a) Water surface elevation is defined at the center of the d' control volume (Figure 3.1).

2. The average of the cell's and all of its *wet* neighbors water surface elevation is higher than the rewetting depth, d_{rewet}, which is equal to or slightly larger than d_{dry}.
3. The average water surface elevation, from 2, is high enough to keep the depth in all of the *wet* neighbors above d_{dry}.

These conditions are similar to those used by Falconer and Chen (1991). The wet/dry state each cell in the domain is checked each hydrodynamic iteration (Section 3.3.1) after the new depth (and water surface elevation) is estimated.

3.8 Bed Accounting

3.8.1 Sediment

The MASS2 sediment bed is represented as a single well-mixed layer with a specified, spatially and temporally constant porosity, p, and variable depth, d_{bed}. The sediment composition of the bed is stored as mass per unit bed area for each sediment fraction, M_{sed_j}. The depth of the bed is computed as

$$d_{\text{bed}} = \rho_b M_{\text{bed}} = \rho_b \sum_{j=1}^{N_{\text{bed}}} M_{\text{sed}_j} \tag{3.35}$$

where M_{bed} is the total sediment mass per unit bed area, and ρ_b is the bed bulk density, computed as

$$\rho_b = \frac{\sum_{j=1}^{N_{\text{sed}}} M_{\text{sed}_j}}{(1-p)\sum_{j=1}^{N_{\text{sed}}} \frac{M_{\text{sed}_j}}{\rho_{s_j}}}$$

where ρ_{s_j} is the solids density for sediment fraction j.

At the end of a simulation time step, the erosion and deposition rates computed during the suspended sediment transport solution (Section 2.3.2) are added and subtracted from the bed mass:

$$M_{\text{sed}_j} = \left(M_{\text{sed}_j}\right)_{\text{old}} + \Delta t \left(D_j - E_j\right) h_1 h_2$$

which is an approximate time integration of the source term in equation 2.12.

3.8.2 Transported Scalars

Transported scalar quantities are also accounted for in the bed, both in a dissolved phase within the bed pore water and particulate phase(s) sorbed to bed sediments. Dissolved scalar quantities are stored as mass per unit bed area, $M_{\phi_{\text{pore}}}$. When necessary, a pore concentration is computed as

$$\phi_{\text{pore}} = \frac{M_{\phi_{\text{pore}}}}{p d_{\text{bed}}}$$

Particulate scalar quantities are also stored as mass per unit bed area, $M_{\phi_{\text{bed}_j}}$. Often, the ratio of scalar to sediment mass is necessary:

$$\phi_{\text{bed}_j} = \frac{M_{\phi_{\text{bed}_j}}}{M_{\text{sed}_j}}$$

At the beginning the simulation time step, scalar mass from non-point sources is added to the bed, as described in Section 3.8.2.2. At the end of the time step, all other direct exchange with the water column is accounted for. This takes two forms. First, any particulate contaminant eroded or deposited with sediment is subtracted or added to the current particulate mass:

$$M_{\phi_{\text{bed}_j}} = \left(M_{\phi_{\text{bed}_j}}\right)_{\text{old}} + \Delta t \left(\frac{D_j \phi_{\text{part}_j}}{\phi_{\text{sed}_j}} - \phi_{\text{bed}_j} E_j\right) h_1 h_2,$$

which is a time integration of the third term of equation 2.15. Second, any exchange of particulate contaminant on the bed surface with the water column is accounted for:

$$M_{\phi_{\text{bed}_j}} = \left(M_{\phi_{\text{bed}_j}}\right)_{\text{old}} + \Delta t \left(\sum_{j=1}^{N_{\text{sed}}} \rho_{s_j} D_{50_j} (1-n) K_{\phi_j} \left(K_{b_{\phi_j}} \phi - \phi_{\text{bed}_j}\right)\right) h_1 h_2,$$

which is a time integration of the third term of equation 2.9.

Those scalar quantities that decay in the water column also decay in the bed. This decay is accounted for at the end of each time step, after any exchange with the water column has been considered. The mass of dissolved scalar quantities are decayed using

$$M_{\phi_{\text{pore}}} = \left(M_{\phi_{\text{pore}}}\right)_{\text{old}} \exp\left(-\lambda_\phi \Delta t\right) \tag{3.36}$$

Similarly, each particulate phase is decayed using

$$M_{\phi_{\text{bed}_j}} = \left(M_{\phi_{\text{bed}_j}}\right)_{\text{old}} \exp\left(-\lambda_\phi \Delta t\right) \tag{3.37}$$

3.8.2.1 Dissolved/Particulate Phase Partitioning

Particulate phase contaminants sorbed to bed sediments are assumed to be instantaneously in equilibrium with their dissolved counterparts in the bed pore water:

$$\phi_{\text{pore}} = \frac{\phi_{\text{bed}_1}}{K_{b_{\phi_1}}} = \frac{\phi_{\text{bed}_2}}{K_{b_{\phi_2}}} = \cdots = \frac{\phi_{\text{bed}_{N_{\text{sed}}}}}{K_{b_{\phi_{N_{\text{sed}}}}}}$$

When written in terms of mass, this becomes

$$\frac{M_{\phi_{\text{pore}}}}{p} = \frac{M_{\phi_{\text{bed}_1}}}{\rho_b K_{b_{\phi_1}} F_1} = \frac{M_{\phi_{\text{bed}_2}}}{\rho_b K_{b_{\phi_2}} F_2} = \cdots = \frac{M_{\phi_{\text{bed}_{N_{\text{sed}}}}}}{\rho_b K_{b_{\phi_{N_{\text{sed}}}}} F_{N_{\text{sed}}}} \tag{3.38}$$

where F_j is the mass fraction of sediment fraction j in the bed. In addition, the total mass of any species ϕ in the bed is

$$M_\phi = M_{\phi_{\text{pore}}} + \sum_{j=1}^{N_{\text{sed}}} M_{\phi_{\text{bed}_j}} = M_{\phi_{\text{pore}}} + \sum_{j=1}^{N_{\text{sed}}} \phi_{\text{bed}_j} M_{sed_j} \tag{3.39}$$

If equation 3.38 is substituted into equation 3.39,

$$M_\phi = M_{\phi_{\text{pore}}} \left(1 + \frac{\rho_b}{p} \sum_{j=1}^{N_{\text{sed}}} K_{d_{\phi_j}} F_j \right)$$

so that the mass of ϕ in the pore water at equilibrium is

$$M_{\phi_{\text{pore}}} = \frac{M_\phi}{1 + \frac{\rho_b}{p} \sum_{j=1}^{N_{\text{sed}}} K_{d_{\phi_j}} F_j} \tag{3.40}$$

and the mass of particulate ϕ at equilibrium is

$$M_{\phi_{\text{bed}_j}} = \phi_{\text{bed}_j} M_{sed_j} = \frac{\rho_b}{p} M_{\phi_{\text{pore}}} K_{d_{\phi_j}} F_j \tag{3.41}$$

where M_ϕ is from equation 3.39.

3.8.2.2 Bed (Non-Point) Source

MASS2 is able to represent non-point sources of contaminants that enter the water body through the bed. The source is described using a mass rate of contaminant entering the bed bottom and a flow rate of groundwater(b) that is carrying the contaminant. As this flux of water and contaminant filter through the bed, the contaminant may sorb to the bed sediments if it has a particulate phase. Once filtered through the bed, contaminant may enter the water column. In the absence of any driving water flux, contaminant in the bed pore water may diffuse into the water column.

To represent these processes, non-point sources are added to the bed in an iterative manner, with a fixed number of iterations performed each time step. At the beginning of each simulation time step, the following algorithm is used:

1. The total contaminant mass, m^*_ϕ, and the average water flux, q_b, to enter the bed from the non-point source is computed.
2. For each iteration:
   (a) A fraction (e.g. 1/3, if there 3 iterations) of m^*_ϕ is added to $M_{\phi_{\text{pore}}}$.
   (b) All phases of ϕ are equilibrated, as described in Section 3.8.2.1.

(b) This additional volume of water is assumed to be very small and is not included in the hydrodynamic solution.

(c) Using the equilibrated pore concentration, the advective and diffusive exchange with the water column is computed and removed from $M_{\phi_{\text{pore}}}$. The rate of exchange with the water column during the i^{th} iteration is computed as

$$q_{\phi_i} = q_b \phi_{\text{pore}} + h_1 h_2 D_{\text{pore}_\phi} \frac{\phi_{\text{pore}} - \phi_{\text{old}}}{0.5 d_{bed}} \tag{3.42}$$

where ϕ_{old} is the water column concentration from the previous time step, D_{pore_ϕ} is a diffusion coefficient.

3. All phases of ϕ are equilibrated again.
4. The computed q_{ϕ_i} are averaged to determine q_ϕ.

The resulting q_ϕ is then used in the solution of scalar ϕ in the water column (equation 2.9).

4.0 Validation Tests

4.1 Hydrodynamic Tests

4.1.1 Subcritical, Uniform Flow in a Rectangular Channel

This test was used to verify that MASS2 was able simulate subcritical uniform open channel flow and does so with multiple computational mesh blocks. The model was configured to simulate a rectangular channel 3048 m (10,000 ft) long and 152.4 m (500 ft) wide (Figure 4.1). A normal depth of 1.524 m (5.0 ft), an average velocity of 0.61 m/sec (2.0 ft/sec), and a Manning's roughness coefficient of 0.026 were chosen. The slope of the channel required to produce these given conditions was predicted with Manning's equation (Chow 1959):

$$S_o = \left[\frac{Vn}{d^{\frac{2}{3}}}\right]^2 \; = \; 1.425 \times 10^{-4} \text{ m/m}$$

Note that the bottom slope was computed using depth rather than wetted perimeter. This is consistent with the representation of bottom friction in MASS2 (Section 2.2), where sidewall friction is not included. The normal depth was applied as the downstream boundary condition. A discharge of 141.6 m^3/sec (5000 cfs) was applied at the upstream boundary.

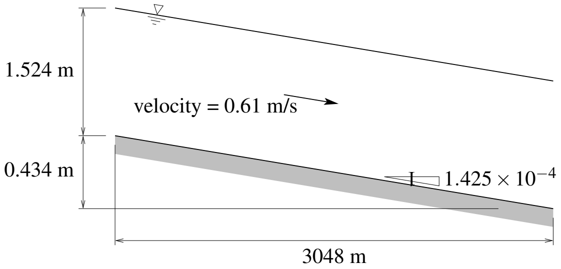

Figure 4.1. Profile dimensions of channel used for subcritical uniform flow in a channel flow test.

Three computational grids were used. The first was a single 100 by 10-cell block. For the second grid, the first was split into two 50 by 10-cell blocks. The third grid consisted of three blocks. A 40 by 10-cell block, having the same resolution as the 1 and 2 block grids, covered the upstream and downstream 1219 m (4000 ft) of the channel. An 80 by 20-cell block, doubling the lateral resolution, was used in the middle 610 m (2000 ft) section of the channel.

MASS2 matched the theoretical depth over the entire length of the channel after starting with a flat water surface profile and zero velocity as initial conditions (Figure 4.2). The steady-state simulated water surface elevation was parallel to the bottom (Figure 4.3). The steady-state simulation was independent of the grid block arrangement.

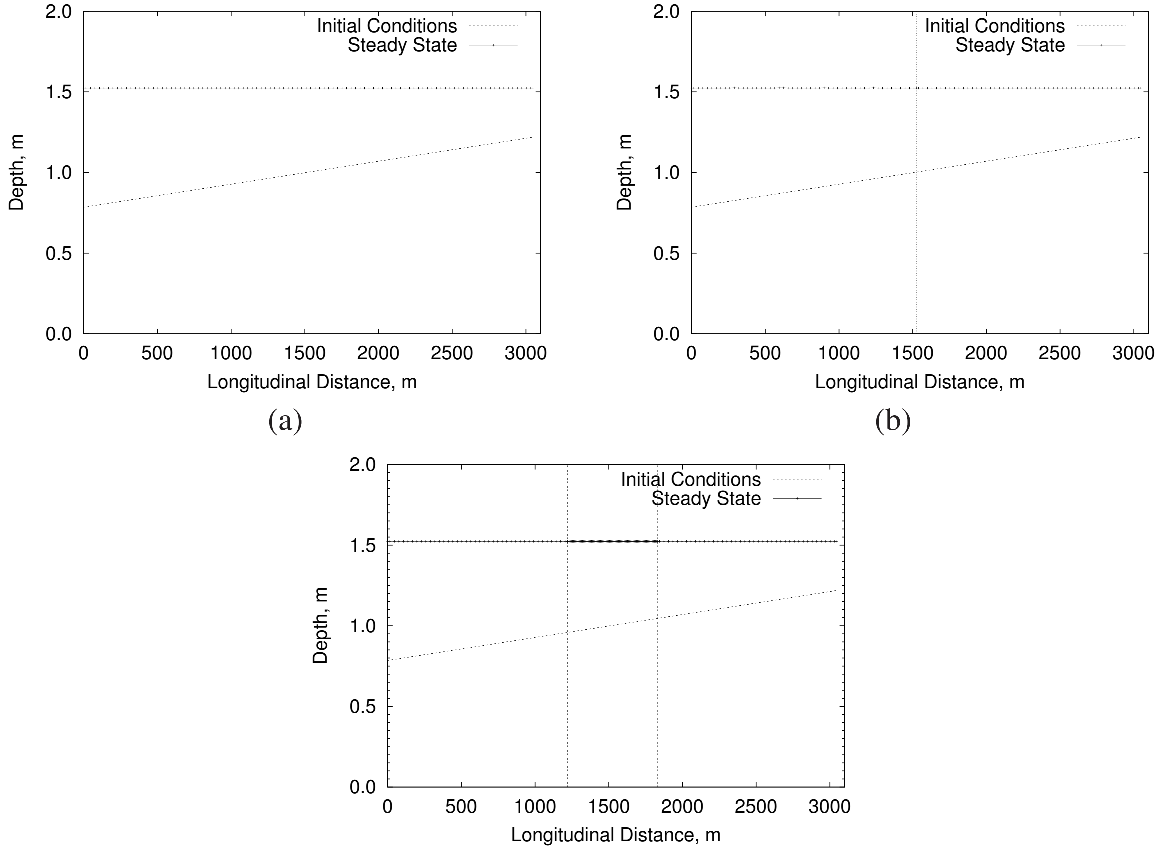

(a) (b)

(c)

Figure 4.2. Simulated steady-state depth profiles from the subcritical uniform flow in a channel tests. Three computational meshes were used: (a) a single 10x100 cell block, (b) two 10x50 blocks, and (c) three blocks with a 10x40 block upstream and downstream and a 20x80 block in between. Vertical lines indicate block boundaries.

4.1.2 Subcritical, Uniform Flow in a Trapezoidal Channel

This test was similar to the test of Section 4.1.1 except that the channel cross section was trapezoidal instead of rectangular. To simulate flow in a trapezoidal channel, MASS2 must use wetting and drying to allow the side slopes to be exposed.

MASS2 was configured to simulate a trapezoidal channel with a base width of 13.4 m (44 ft) and a side slope of 0.08929. The channel was chosen to be 30.5 m (100 ft) wide by 1.52 m (5 ft) deep overall (Figure 4.4) and 305 m (1000 ft) long. A single block, 50 by 25-cell mesh was used. A constant discharge of 40.8 m^3/sec (1440 ft^3/sec) was imposed at the upstream end. Manning's roughness coefficient was set to 0.026 and the longitudinal slope was set to 1.6025^{-3}, which was expected to result in a normal depth of 1.22 m (4.0 ft). Initially, the water surface elevation was set to inundate the entire mesh 2.74 m (9 ft). The center line depth imposed at the downstream boundary started at the initial value and was gradually decreased to the expected normal depth, where it remained for the duration of the simulation. The dry and rewetting depths used were very small: 3.05×10^{-3} m (0.01 ft) and 3.66×10^{-3} m (0.012 ft), respectively.

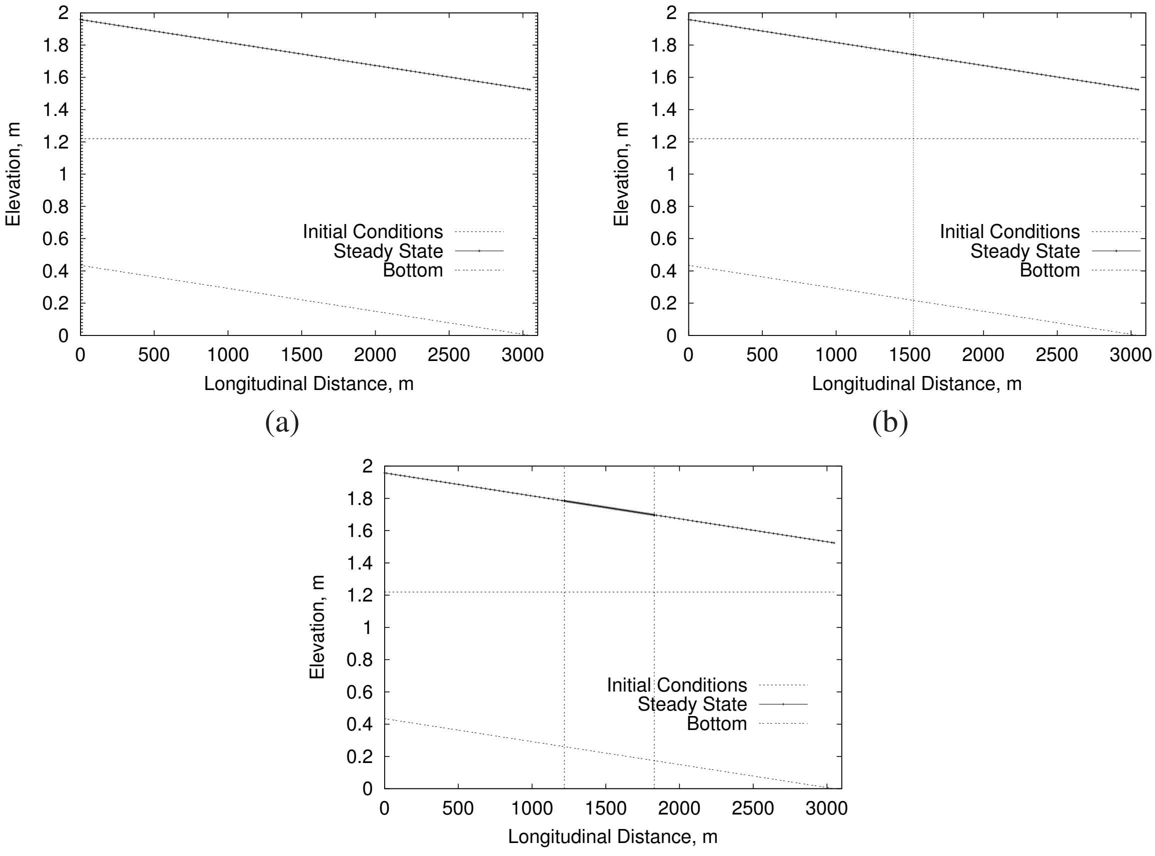

(a) (b)

(c)

Figure 4.3. Simulated steady-state water surface elevation profiles from the subcritical uniform flow in a rectangular channel tests. Three computational meshes were used: (a) a single 10x100 cell block, (b) two 10x50 blocks, and (c) three blocks with a 10x40 block upstream and downstream and a 20x80 block in between. Vertical lines indicate block boundaries.

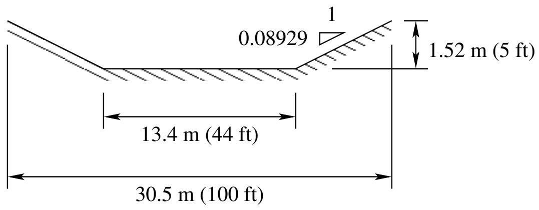

Figure 4.4. Channel cross section used for the uniform flow in a trapezoidal channel test.

The center line flow depth simulated by MASS2 was very close to that expected (Figure 4.5). Depth was slightly over-predicted at the upstream end of the channel, probably due to the inexact imposition of the discharge at the boundary.

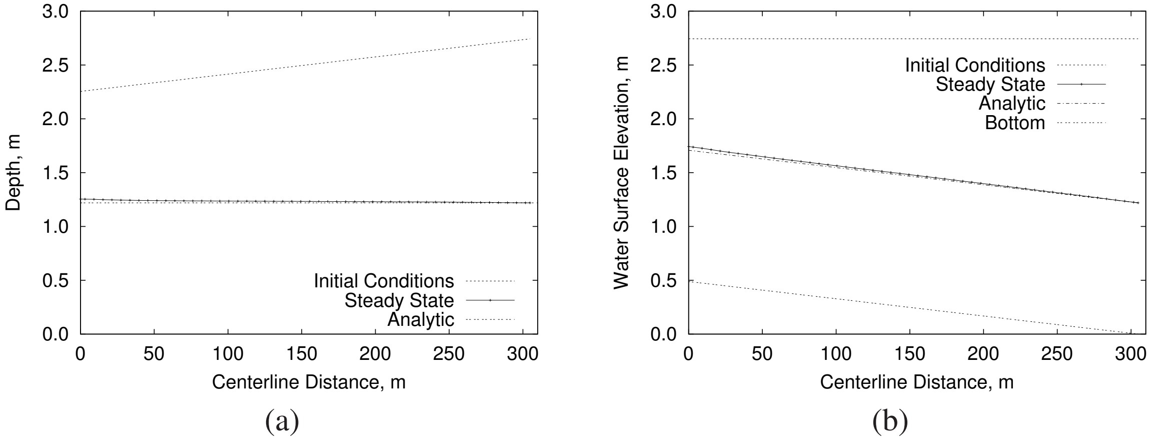

(a) (b)

Figure 4.5. Comparison of simulated depth (a) and water surface elevation (b) from the subcritical, uniform flow in a trapezoidal channel.

4.1.3 Gradually Varied Subcritical Flow in a Rectangular Channel

In this test, the channel used in Section 4.1.1 was extended to double its length in two ways (Figure 4.6). In case 1, the extension was placed downstream of the original channel. The slope of this extension was made steeper than the original channel, $S_o = 1.4208 \times 10^{-3}$, so that the expected flow would be subcritical, with a depth of 0.762 m (2.5 ft), a velocity of 1.22 m/sec (4 ft/sec), and a channel discharge of 141.6 m^3/sec (5000 cfs). In case 2, the steeper extension was placed upstream of the original channel.

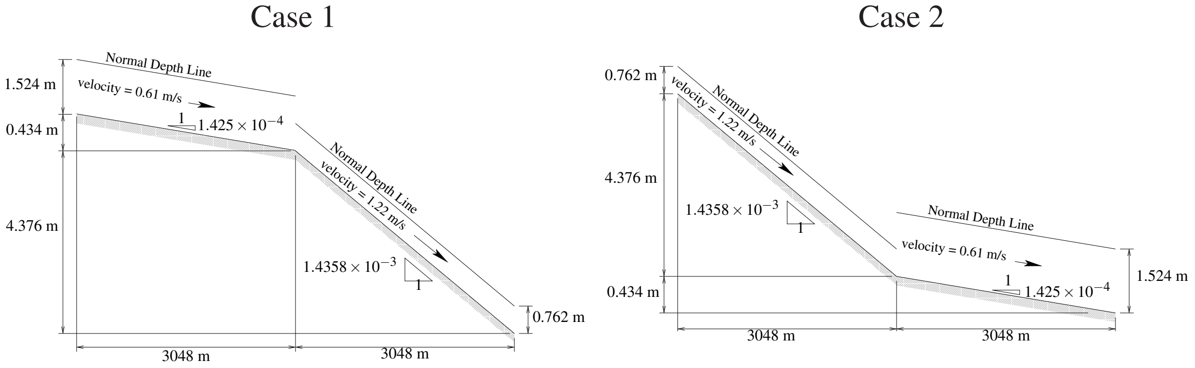
Case 1

Case 2
Normal Depth Line
velocity = 0.61 m/s
1.524 m
0.434 m
1
1.425 × 10^-4
Normal Depth Line
velocity = 1.22 m/s
4.376 m
1.4358 × 10^-3
1
0.762 m
3048 m
3048 m
0.762 m
Normal Depth Line
velocity = 1.22 m/s
4.376 m
1.4358 × 10^-3
1
Normal Depth Line
velocity = 0.61 m/s
0.434 m
1
1.425 × 10^-4
1.524 m
3048 m
3048 m

Figure 4.6. Dimensions of channel used for the gradually varying flow in a channel tests.

MASS2 was configured to simulate each of these cases with a 200 by 10-cell single-block grid. The channel discharge was imposed as the upstream boundary condition and the expected normal depth was imposed as the downstream boundary condition. The simulations were started with a constant depth and of 0.91 m (3.0 ft) a longitudinal velocity of 0.061 m/sec (0.2 ft/sec).

In both cases, normal depth in the downstream reach was simulated as expected (Figure 4.7). In case 2, the expected normal depth was also simulated in the upper reach. In case 1, however, the upper reach was not long enough to obtain normal depth to become established. Instead, a classic M2 profile (Chow 1959) was simulated where depth was in transition to the shallower downstream depth.

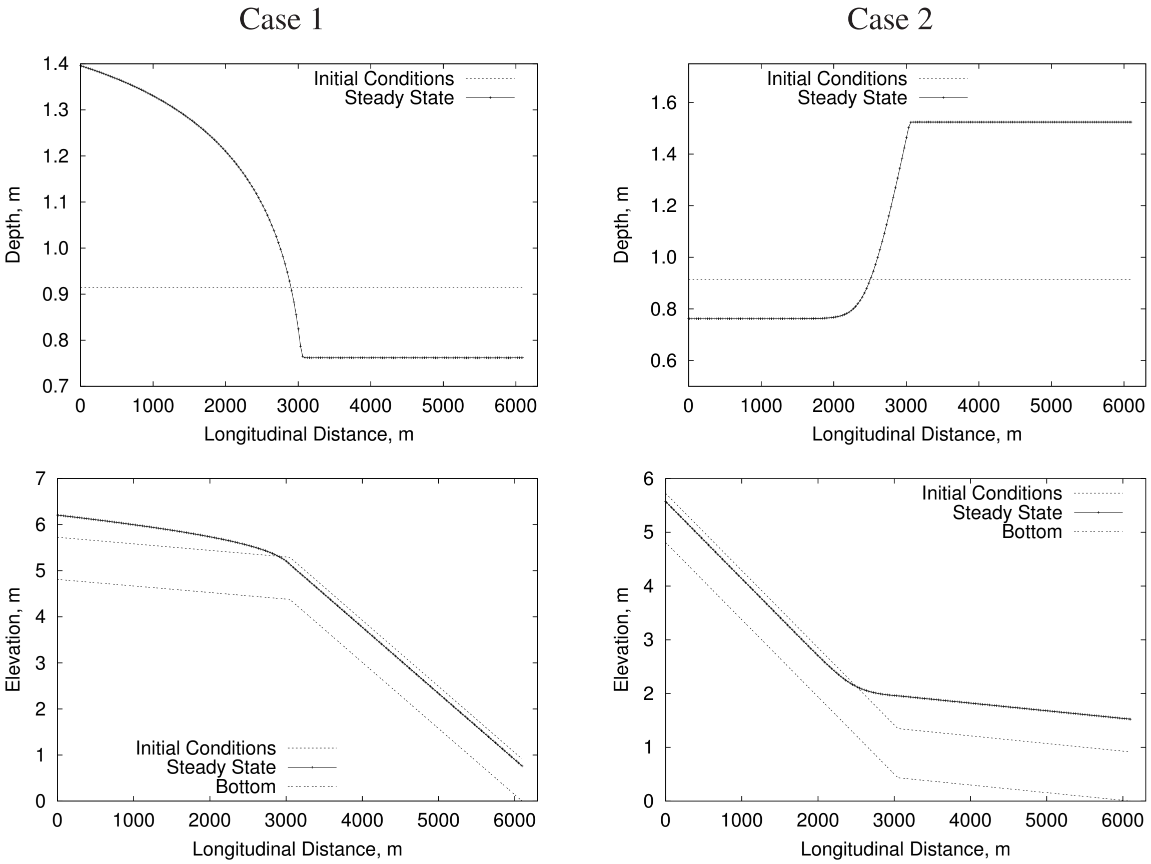

Figure 4.7. Simulated steady-state depths and water surface elevations from the gradually varied flow in a rectangular channel test.

4.1.4 Transition to Supercritical Flow in a Rectangular Channel

This test validates MASS2 in two ways: simulation of supercritical flow and the use of a zero gradient hydrodynamic downstream boundary condition. MASS2 was configured to simulate a channel 5000 ft long. The upstream 1220 m (4000 ft) of the channel had the same dimensions as the channel used in Section 4.1.1. The lower 152 m (500 ft) had the same rectangular section but a bottom slope of 0.0676 m/m. With a channel discharge of 142 m^3/sec (5000 cfs) and Manning roughness coefficient of 0.026, the expected normal depth in the supercritical part of the channel would be 0.240 m (0.787 ft) and the velocity would be 3.87 m/sec (12.7 ft/sec). Critical depth for this channel was 0.445 m (1.459 ft).

The channel was simulated with a single block grid 140 cells long by 10 cells wide. The upstream, subcritical portion used 40 cells longitudinally and the downstream, supercritical portion used 100 cells. A depth of (5 ft) and a zero velocity were supplied as initial conditions.

The simulated water surface profile displays the classic M2 profile (Chow 1959) while transitioning from subcritical to critical (Figure 4.8). The location of critical depth was correctly simulated to be where the slope changed. The classic S2 profile was simulated downstream where flow transitioned from critical to supercritical.

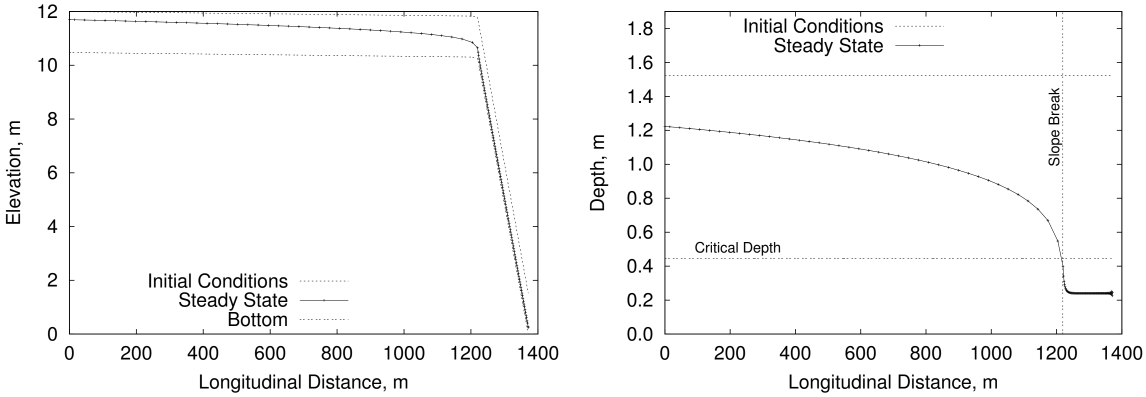

Figure 4.8. Simulated steady-state water surface elevation and depth from the transition to supercritical flow in a rectangular channel test.

4.1.5 Hydraulic Jump in a Straight Channel

This test was used to examine the ability of the model to simulate the transition of flow from supercritical to subcritical with a hydraulic jump. Gharangik (1988) performed measurements of such a transition in a laboratory flume. The model was configured to simulate a rectangular channel 0.45 m (1.48 ft) wide and 13.9 m (45.60 ft) long using a single 238 by 5-cell grid block. The channel had no bottom slope. A depth of 0.064 m (0.21 ft) and velocity of 1.82 m/sec (5.97 ft/sec) were imposed at the upstream boundary, resulting in a channel discharge of 0.053 m^3/sec (1.87 cfs) and upstream Froude number of 2.30. A velocity of 0.69 m/sec (2.264 ft/sec) was imposed at the downstream end resulting in a depth of 0.17 m (0.58 ft) and a Froude number of 0.53. The initial conditions were a depth of 0.064 m (0.21 ft) and a velocity of 0.34 m/sec (1.0 ft/sec) longitudinally and zero laterally.

The model simulated depths very similar to the laboratory experiment (Figure 4.9). The simulated jump was correctly located, but the simulated jump was steeper and also somewhat smoother than the observed. Several simulations were performed to identify correct values for Manning roughness coefficient and eddy viscosity. The simulated jump was very sensitive to both of these values. A value of 0.007 was chosen, which was slightly below the range measured in the experiments (0.008 to 0.011). The eddy viscosity was chosen to be 0.074 m^2/sec (0.8 ft^2/sec).

4.1.6 Varied Flow in a Trapezoidal Channel

MacDonald et al. (1997) presented analytic solutions to a set of gradually and rapidly open channel flow problems. Their test problem 3 considered subcritical flow in a channel with a varying bottom slope. The channel was 5 km (3.1 miles) long with a Manning roughness coefficient of 0.030 and a trapezoidal section with a base width of 10 m (32.8 ft) and a 1:2 side slope. The

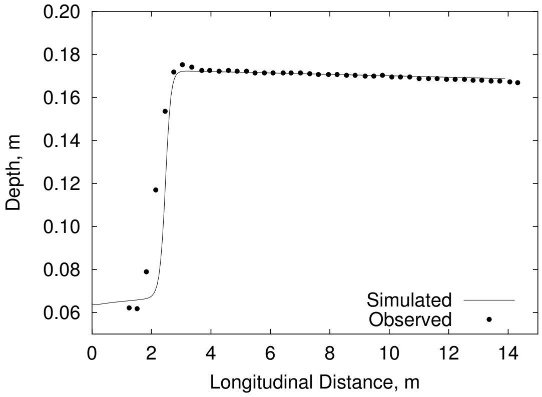

Figure 4.9. Simulated depth from the hydraulic jump in a straight channel test compared to that observed by Gharangik (1988).

channel discharge was 20 m^3/sec (707.3 cfs) and the downstream depth was 1.125 m (3.69 ft). The bottom slope was given by

$$S_o = \left\{1 - \frac{400\,[10+4d(x)]}{g\,[10+2d(x)]^3\,d(x)^3}\right\} d'(x) \;+\; 0.36\frac{\left[10+2d(x)\sqrt{5}\right]^{4/3}}{[10+2d(x)]^{10/3}\,d(x)^{10/3}}$$

where slope, S_o, and hydraulic depth, $d(x)$, are functions of distance along the channel, x, and g is gravitational acceleration. The depth and its derivative is given by

$$d(x) = \frac{9}{8} + \frac{1}{4}\sin\left(\frac{\pi x}{500}\right) \tag{4.1}$$

and

$$d'(x) = \frac{\pi}{2000}\cos\left(\frac{\pi x}{500}\right)$$

The solution to the problem is given by equation 4.1. MASS2 was configured to simulate this problem using a 2500 by 24 cell grid that was 18 m (59.1 ft) wide. This grid would allow depths up to 2 m without exceeding the top of trapezoidal section. The dry and rewetting depths used were very small: 1.52×10^{-3} m (0.005 ft) and 1.83×10^{-3} m (0.006 ft), respectively.

Depths simulated by MASS2 were consistent with, but slightly lower than, the analytic solution (Figure 4.10). This is probably due to the representation of friction in MASS2 (Section 2.2). MASS2 friction is based on the bed area projected to a horizontal plane, whereas the analytic solution uses the wetted perimeter. Consequently, friction on the sides of the trapezoidal section was slightly underestimated.

Test problem 4 of MacDonald et al. (1997) considered flow in a trapezoidal channel transitioning from subcritical to supercritical and the transitioning back to subcritical with a hydraulic jump. The channel was 1000 m (3280 ft) long with a Manning roughness coefficient of 0.020. The channel cross section had a base width of 10 m (3.28 ft) and a 1:1 side slope. The channel discharge was 20 m^3/sec (707.3 cfs), and the depth at the downstream boundary was 1.349963 m

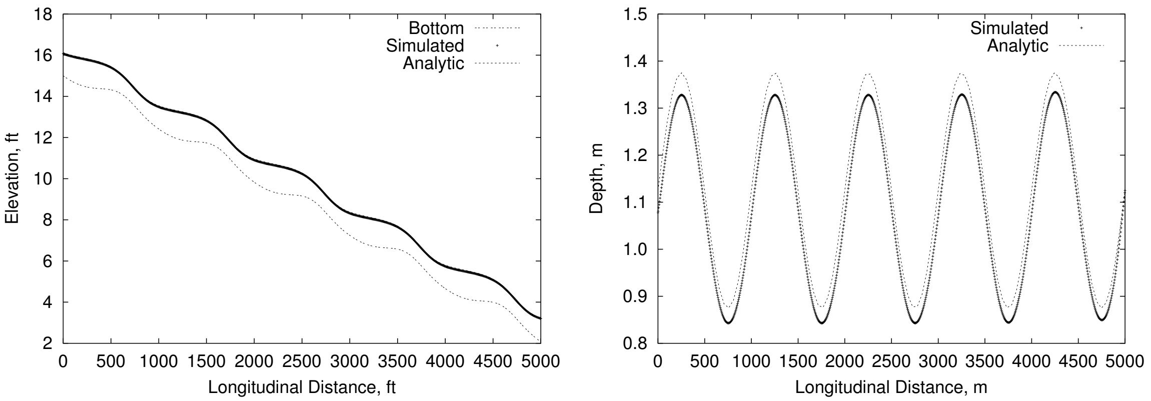

Figure 4.10. Simulated water surface elevation and depth compared with the analytic solution to problem 3 of MacDonald et al. (1997).

(4.429 ft). The channel slope was given by

$$S_o(x) \;=\; \left\{1-\frac{400\left[10+2d(x)\right]}{g\left[10+d(x)\right]^3 d(x)^3}\right\}d'(x)+0.16\frac{\left[10+2d(x)\sqrt{(2)}\right]^{4/3}}{\left[10+d(x)\right]^{10/3}d(x)^{10/3}}$$

where

$$d(x) \;=\; \begin{cases} 0.723449\left[1-\tanh\left(\dfrac{x}{1000}-\dfrac{3}{5}\right)\right] & \text{for } 0\le x\le 300\\ 0.723449\left\{1-\dfrac{1}{6}\tanh\left[6\left(\dfrac{x}{1000}-\dfrac{3}{5}\right)\right]\right\} & \text{for } 300< x\le 600\\ \dfrac{3}{4}+\displaystyle\sum_{k=1}^{3}a_k\exp\left[-20k\left(\dfrac{x}{1000}-\dfrac{3}{5}\right)\right]+\dfrac{3}{5}\exp\left(\dfrac{x}{1000}-1\right) & \text{for } 600< x\le 1000 \end{cases}$$

which is the solution, and

$$d(x) \;=\; \begin{cases} -0.723449\times 10^{-3}\operatorname{sech}^2\left(\dfrac{x}{1000}-\dfrac{3}{10}\right) & \text{for } 0\le x\le 300\\ -0.723449\times 10^{-3}\operatorname{sech}^2\left[6\left(\dfrac{x}{1000}-\dfrac{3}{10}\right)\right] & \text{for } 300< x\le 600\\ -\dfrac{1}{50}\displaystyle\sum_{k=1}^{3}ka_k\exp\left[-20k\left(\dfrac{x}{1000}-\dfrac{3}{5}\right)\right]+\dfrac{3}{5000}\exp\left(\dfrac{x}{1000}-1\right) & \text{for } 600< x\le 1000 \end{cases}$$

where $a_1=-0.111051$, $a_2=0.026876$, and $a_3=-0.217567$.

MASS2 was configured to simulate this case using a 500 by 56-cell grid. The dry and rewetting depths used were very small: 3.05×10^{-3} m (0.01 ft) and 3.66×10^{-3} m (0.012 ft), respectively. Depths simulated by MASS2 were very close to the analytic solution (Figure 4.11). The hydraulic jump was simulated in the expected location; depths above the hydraulic jump were slightly overestimated.

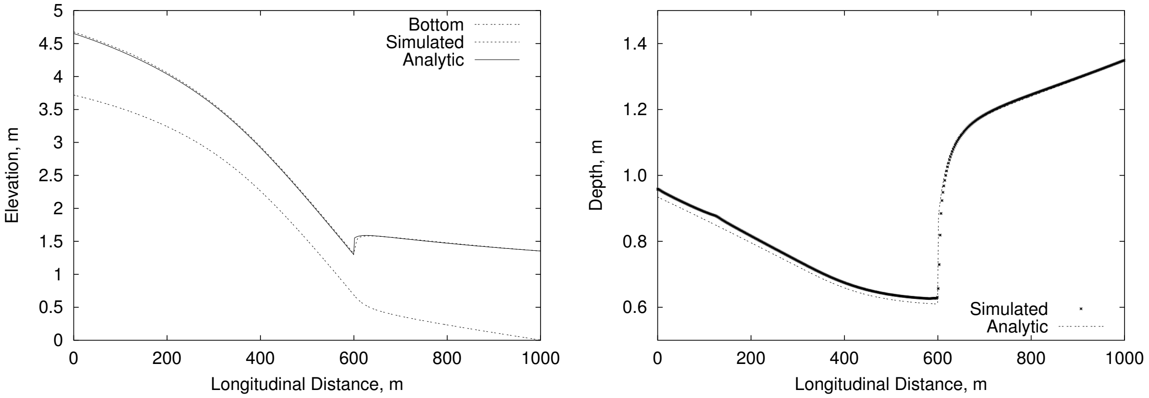

Figure 4.11. Simulated water surface elevation and depth compared with the analytic solution to problem 4 of MacDonald et al. (1997).

4.1.7 Flow in a Converging and Diverging Channel

Panagiotopoulos and Soulis (2000) and Klonidis and Soulis (2001) describe a laboratory study of subcritical flow in a converging and diverging flume. The flume was 0.25 m (0.82 ft) wide at the entrance and exit and narrowed to half that width in between (Figure 4.12). Velocity and depth measurements were taken along approximate streamlines that divided the flume laterally in fifths.

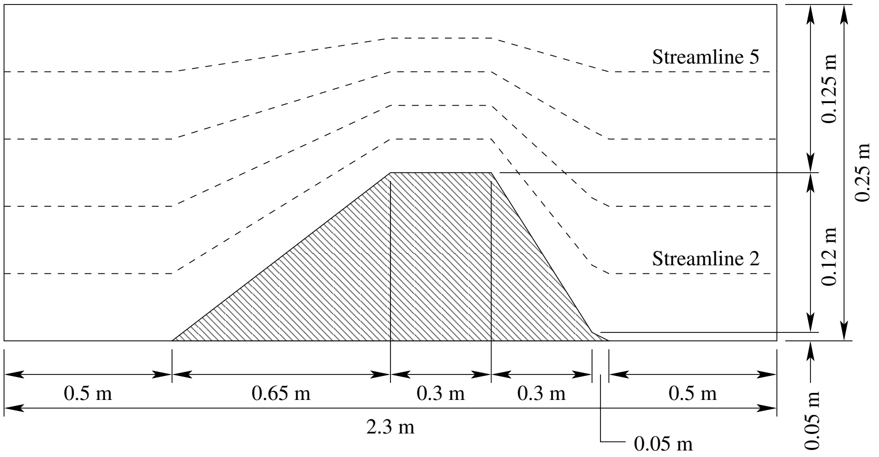

Figure 4.12. Model domain used to represent the converging and diverging channel test. The dashed lines denote the approximate streamlines along which measurements were made.

MASS2 was configured to simulate this flume using a 50 by 10-cell mesh. A discharge of 0.286 m^3/sec (0.727 ft^3/sec) was imposed as the upstream boundary condition. A depth of 0.286 m (0.938 ft) was imposed as the downstream boundary condition, based on observations. Simulated depths and velocities were compared with observations made along the approximate streamlines 2 and 5 (Figure 4.12). Manning's roughness coefficient was set to 0.010. Several values of eddy viscosity were tested; a value of 0.014 m^2/sec (0.15 ft^2/sec) produced the best results. Simulated depths were consistent with the observed and with the previous simulation of Klonidis and Soulis (2001) (Figure 4.13).

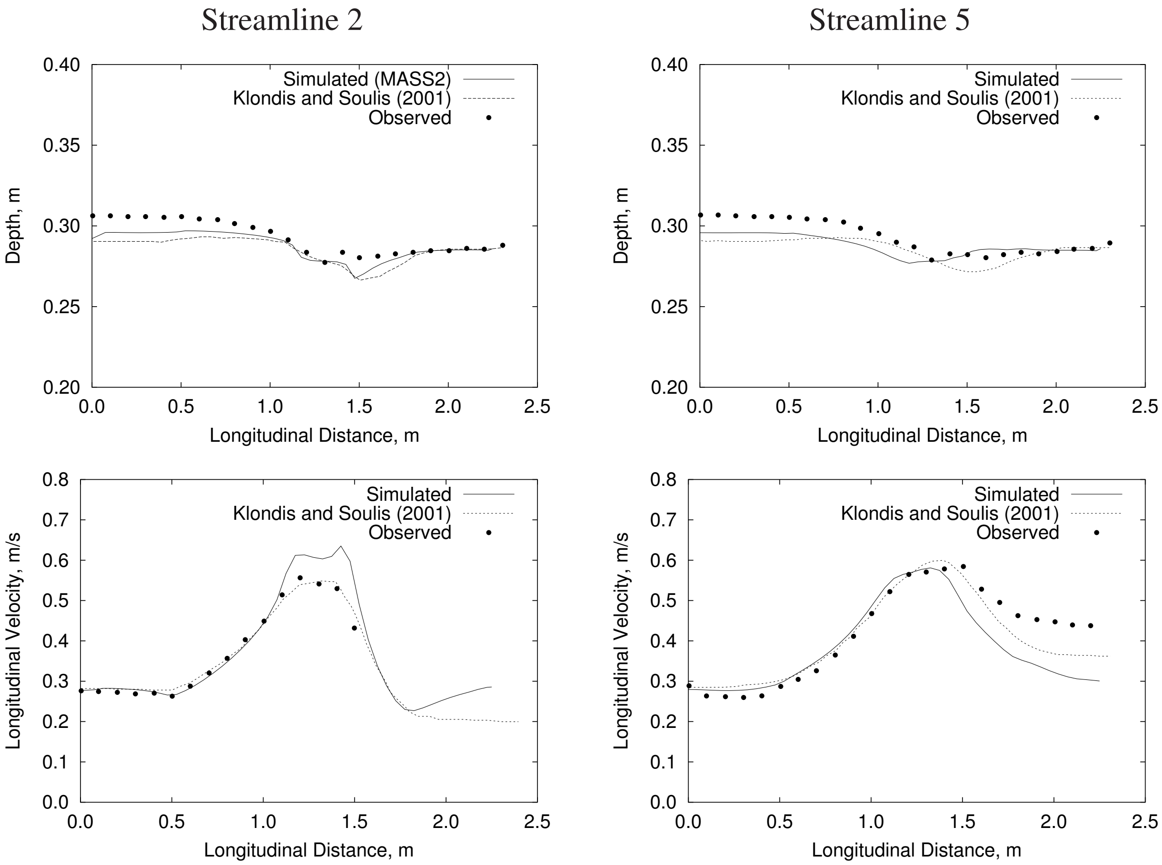
Streamline 2

Streamline 5

Figure 4.13. Simulated depth and velocity in the converging and diverging channel test compared with that observed by Panagiotopoulos and Soulis (2000).

4.1.8 Two-Dimensional Flow Around a Spur Dike

Flow around a spur-dike, or groyne, has been used in several studies to verify hydrodynamic models (Ouillon and Dartus 1997; Tingsanchali and Maheswaran 1990; Molls and Chaudhry 1995). Tingsanchali and Maheswaran (1990), Molls and Chaudhry (1995) and Molls et al. (1995) compared simulations to the data of Rajaratnam and Nwachukwu (1983) and Nawachukwu (1979). Ouillon and Dartus (1997) compared simulation against another set of experimental data. This test compared flow simulated by MASS2 with the experimental work done by Rajaratnam and Nwachukwu (1983). The Manning's roughness coefficient was set to 0.010.

The domain dimensions are shown in Figure 4.14. The spur-dike was represented as a very thin plate using a wall internal boundary (Section 3.5). This constitutes a slip condition for the lateral velocity at the wall. After several simulations were performed with varying eddy viscosity, a value of 1.50 m^2/sec (1.61e-02 ft^2/sec) was chosen.

Under these conditions, MASS2 simulated a recirculation zone behind the spur-dike about 1.7 m long (Figure 4.15). The slip condition at the spur-dike was apparent (Figure 4.16). The variation of longitudinal velocity at relative distances across the channel were compared with observed (Figure 4.17). In general, the velocities simulated by MASS2 were consistent with observations.

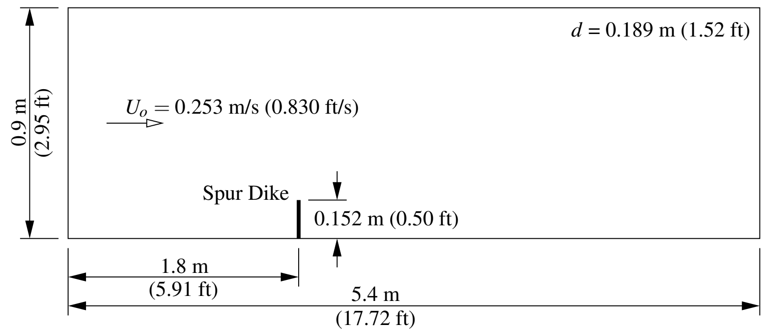

d = 0.189 m (1.52 ft)
0.9 m (2.95 ft)
U_o = 0.253 m/s (0.830 ft/s)
Spur Dike
0.152 m (0.50 ft)
1.8 m (5.91 ft)
5.4 m (17.72 ft)

Figure 4.14. Computational domain for the flow around a spur-dike test.

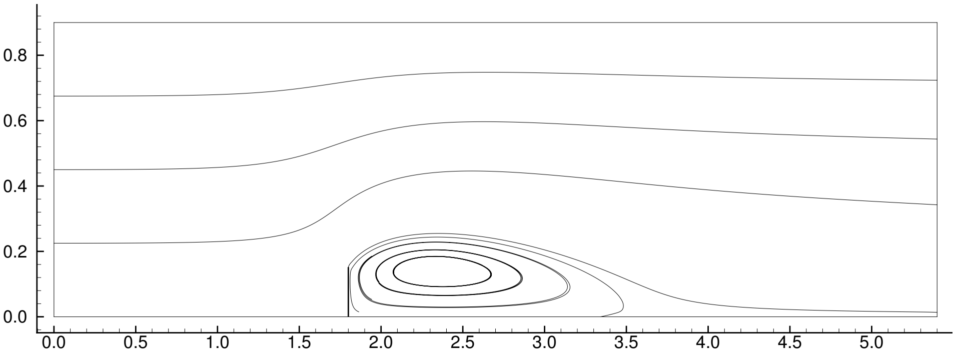

Figure 4.15. Streamlines from the flow around a spur dike test.

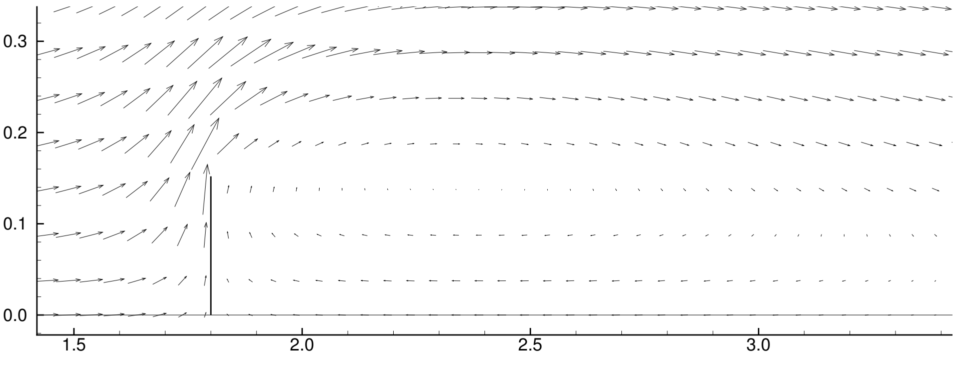

Figure 4.16. Simulated velocity vectors near the spur-dike. Every other vector is shown.

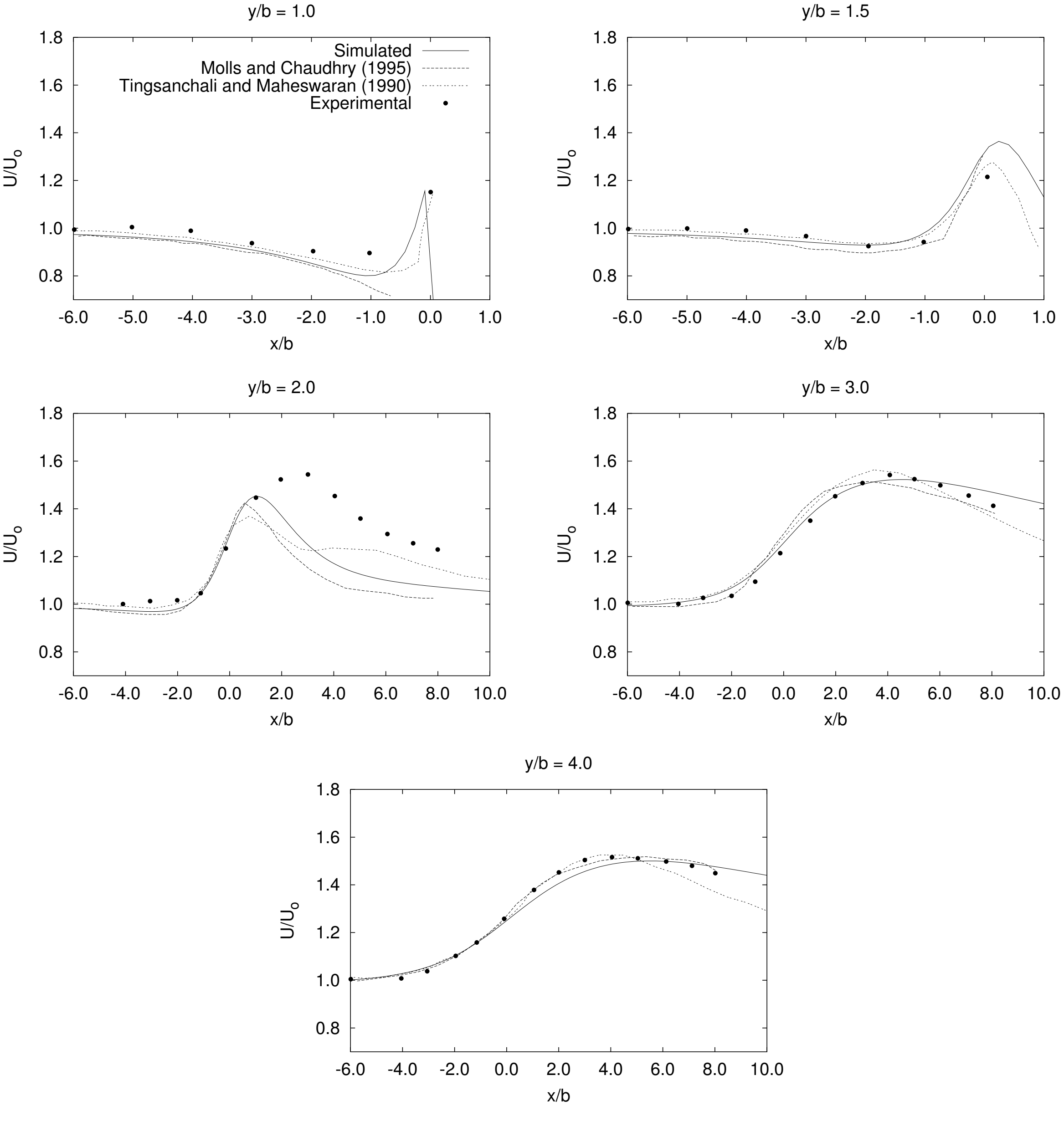

Figure 4.17. Comparison of simulated velocity with observed and other reported simulations of the flow around a spur-dike test. *y* is the distance across the

4.1.9 Side Discharge into an Open Channel

This test was used to compare MASS2 with experimental work done by Rodi and Weiss (1980) (as presented by Ye and McCorquodale 1997). The model was configured to simulate a rectangular channel with width, *B*, of 1.82 m (5.971 ft), a length of 4*B*, 7.28 m (23.884 ft), and zero slope (Figure 4.18). The initial and downstream boundary depth were 0.06 m (0.197 ft). The entire domain was assigned a value of 0.0001 for Manning's roughness coefficient, *n*, to represent a smooth surface. A constant discharge of 0.1092 m^3/sec (0.3856 ft^3/sec) to produce an average longitudinal velocity $\left(\overline{U}\right)$ of 0.1 m/sec (0.328 ft/sec). After several simulations were performed with varying eddy viscosity, a value of 9.29×10^{-3} m^2/sec (1.00×10^{-2} ft^2/sec) was chosen.

According to the summary of previous data and simulation presented by Ye and McCorquodale (1997), the recirculation zone caused by the jet should be 1 to 1.7 times *B* in length and about 0.2 times in width. The size of recirculation zone simulated by MASS2 had dimensions close to these (Figure 4.19).

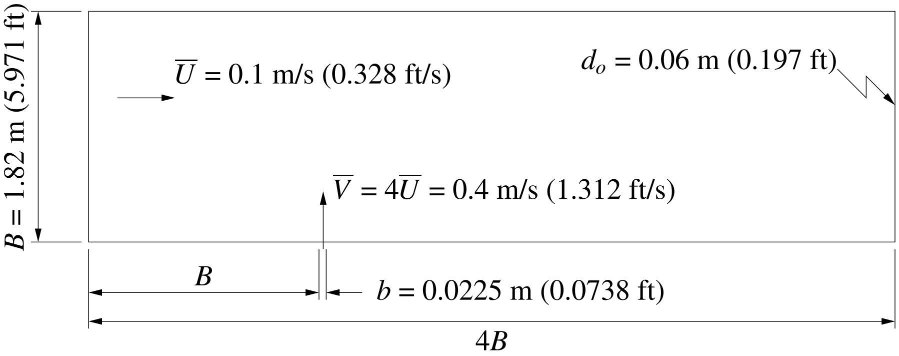
B = 1.82 m (5.971 ft)
$\overline{U}$ = 0.1 m/s (0.328 ft/s)
d_o = 0.06 m (0.197 ft)
$\overline{V} = 4\overline{U}$ = 0.4 m/s (1.312 ft/s)
B
b = 0.0225 m (0.0738 ft)
4B

Figure 4.18. Model domain and boundary conditions for the side discharge into an open channel test.

4.1.10 Flow in a Meandering Channel

Chang (1971) performed several experiments in a flumes with one or more meanders. The large flume was 7.67 ft wide and consisted of two opposing 3.0-ft-radius, 90-degree bends connected by a straight section of 18.75 ft. The experiment was performed with a uniform flow in the flume with a depth of 0.377 ft (0.115 m) and a bulk velocity of 1.2 ft/sec (0.366 m/sec). To provide uniform flow, the flume was tilted at a slope of 3.5×10^{-4} ft/ft. This not the slope of the channel, but of the table supporting the flume. Chang (1971) measured velocity along four cross sections labeled A, B, C, and D in Figure 4.20.

MASS2 was configured to represent the large flume experiment performed by Chang (1971). The MASS2 configuration used the domain shown in Figure 4.20. A constant, evenly distributed discharge of 3.478 ft^3/sec (0.0985 m^3/sec) was imposed as the upstream boundary condition. A constant stage was imposed at the downstream boundary, leading to constant depth of 0.377 ft at the center of the channel. After several test simulations with varying values, Manning's *n* was chosen to be 0.01125 so that the upstream and downstream depths were nearly the same.

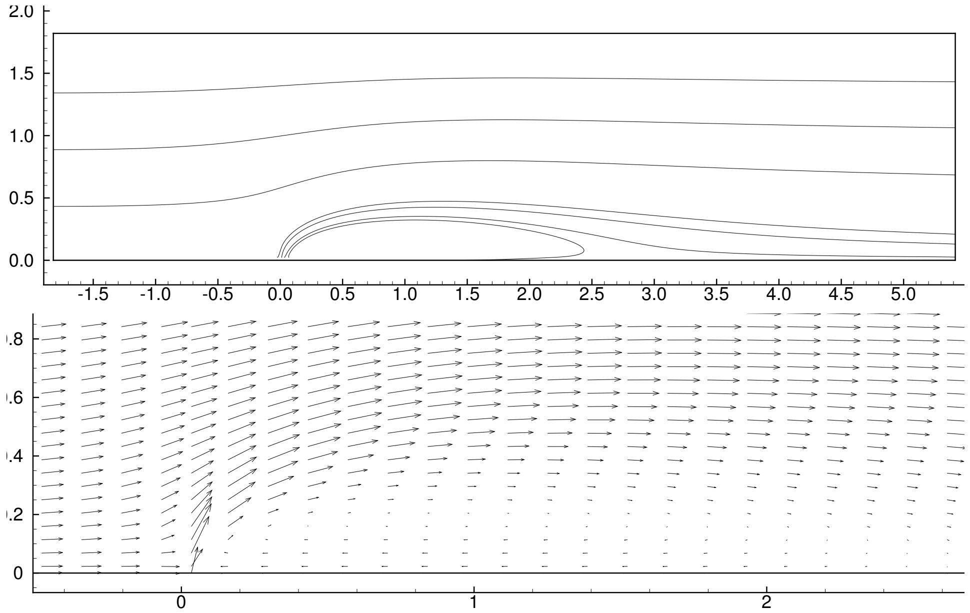

Figure 4.19. Simulation results from the side discharge into an open channel test. Streamlines (above) are shown for the entire domain. Velocity vectors are shown only in the vicinity of the jet (longitudinally, every third vector is shown).

Simulated velocity varied linearly across flume (Figures 4.21 and 4.22). Measured velocity appeared to be heavily influenced by the side wall (Figure 4.22). To try to emulate this, a second simulation was performed but with Manning's roughness coefficient much higher (0.040) in the cells along the flume walls and slightly lower (0.00925) elsewhere. Simulated upstream and downstream depths were nearly the same with this combination. This helped bring simulated velocities near the walls closer to those measured (Figure 4.22).

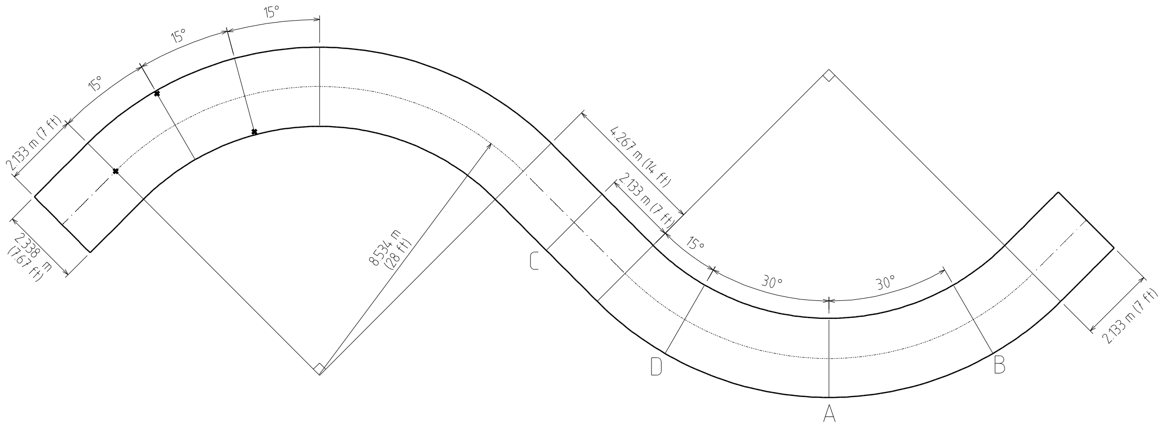

Figure 4.20. Dimensions of the simulation domain used in the meandering channel test.

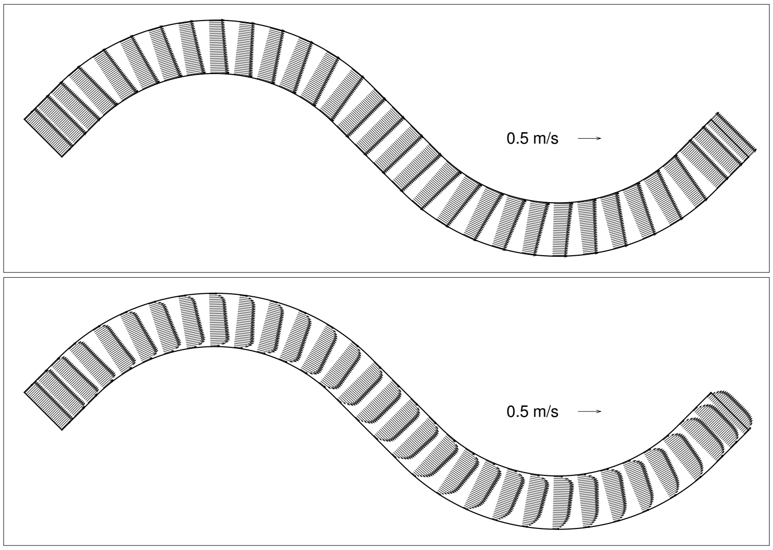

Figure 4.21. Simulated velocity vectors in the meandering channel test case. The upper graph shows vectors from the simulation using the slip boundary condition along the channel walls. The lower graph shows vectors from the simulation with increased roughness at the walls.

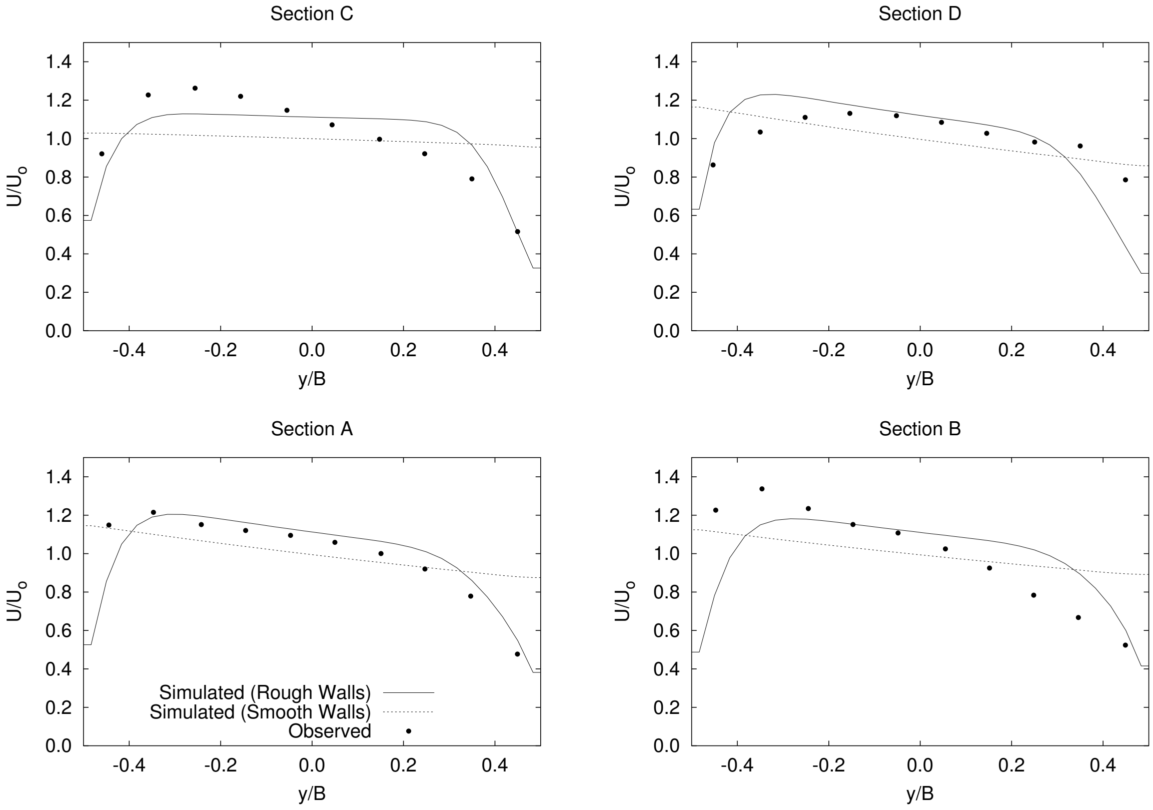

Figure 4.22. Comparison of simulated and observed velocity at the sample sections in the flow in a meandering channel test.

4.2 General Scalar Transport Tests

4.2.1 One-Dimensional Advection

This tests the longitudinal transport of an arbitrary species by advection only. It exercises the scalar transport capabilities of MASS2 and highlights some shortcomings of the underlying transport algorithm in unsteady simulations where sharp gradients of the transported quantity occur. For unsteady simulations the power-law advection scheme will yield solutions that are overly diffusive. As noted by Patankar (1980), the nature of numerical or false diffusion in unsteady simulations is different than in multi-dimensional steady-state simulations where the performance of the power-law scheme is adequate when the computational grid is aligned with the flow streamlines.

The channel configuration described in Section 4.1.1 was used. A triangular pulse of contaminant concentration, shown in Figure 4.23, was used as a boundary condition, which can be described as

$$\phi_o(t) = \begin{cases} 0 & \text{for } t \leq 0, \\ \phi_p \left(1 - \dfrac{t_p - t}{t_p}\right) & \text{for } 0 < t \leq t_p, \\ \phi_p \left(1 - \dfrac{t - t_p}{t_p}\right) & \text{for } t_p < t \leq 2t_p, \\ 0 & \text{for } t > 2t_p \end{cases} \tag{4.2}$$

where t is time measured from start of the pulse (06:00 in Figure 4.23), t_p is the time to the peak (24 min), and ϕ_p is the peak concentration (10.0). With pure advection, this pulse should be translated downstream without change in shape. The translated concentration is

$$\phi(x,t) \;=\; \phi_o(t - x/v) \tag{4.3}$$

where x is the distance along the channel and v is the flow velocity (2.0 ft/sec in this case). Several simulation time steps were used in order to test the effect of varying Courant number, C_n, given by

$$C_n = \frac{v\Delta t}{\Delta x}$$

Time steps were chosen to produce Courant numbers of 0.1, 1.0, and 6.0.

Solution of the transport equation in MASS2 was highly diffusive in this unsteady problem (Figure 4.24). The sharp concentration pulse was reduced considerably as it traveled downstream. The reduction of the peak concentration was greatest with the Courant number of 6.0 and some phase error is also apparent in the simulation.

4.2.2 One-Dimensional Advective Diffusion

This test compared MASS2 (longitudinal) transport simulation to an analytic solution to the unsteady advection-diffusion equation. The analytic solution describes the transport of a sharp concentration front through a medium moving at a constant velocity and having an initial concentration of zero. The concentration along the channel is described as (Fischer et al. 1979)

$$C(x,t) = \frac{C_o}{2}\left[1 - \operatorname{erf}\left(\frac{x - vt}{\sqrt{4K_T t}}\right)\right] \tag{4.4}$$

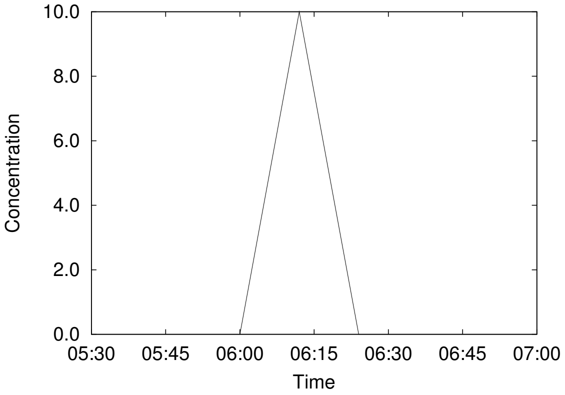

Figure 4.23. Upstream concentration boundary condition used for the one-dimensional advection test. The time axis is shown in 24-hour clock time. Simulation start time was 05:00.

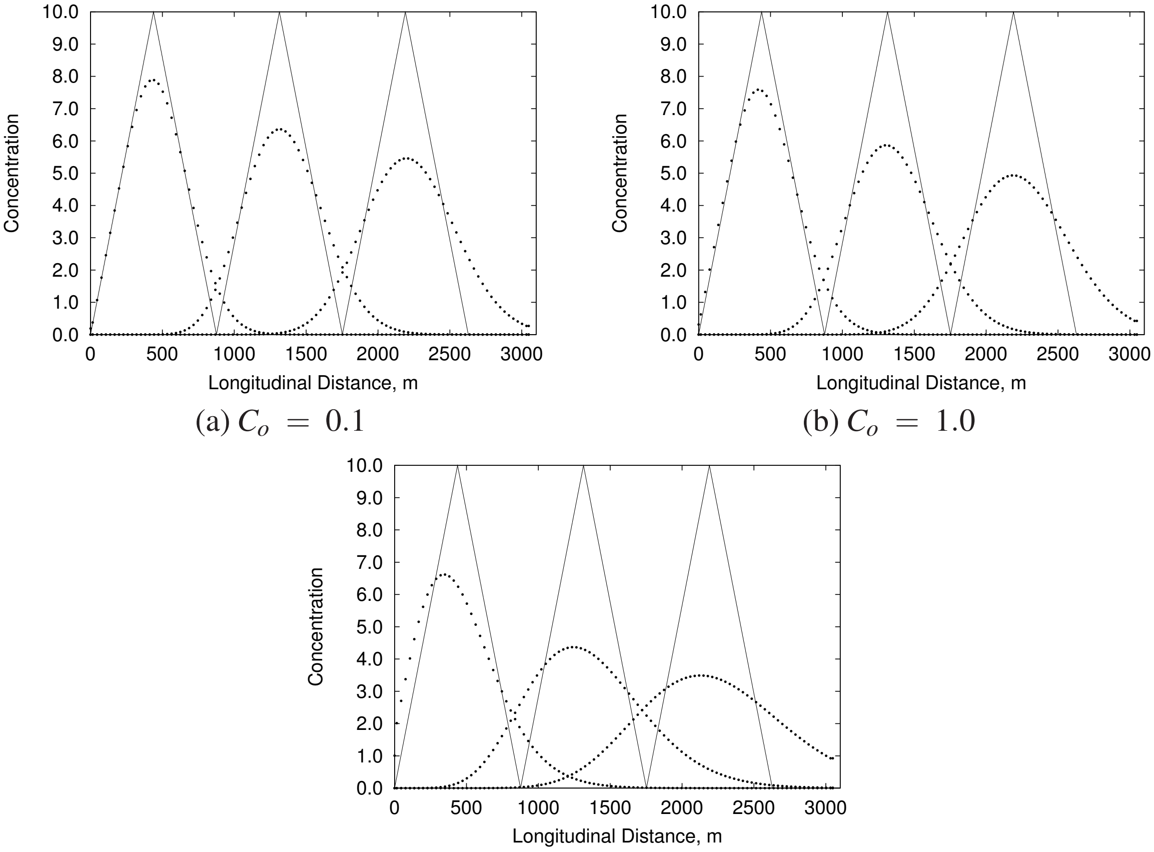

(a) $C_o = 0.1$

(b) $C_o = 1.0$

(c) $C_o = 6.0$

Figure 4.24. Results of the one-dimensional advection test for three Courant numbers: (a) 0.1, (b) 1.0, and (c) 6.0. The plots show simulation results (points) and the advected boundary concentration (4.3, solid line) at 24, 48 and 72 minutes after the concentration peak at the upstream boundary.

where t is time, x is the distance along the channel, v is the flow velocity, C_o is the height of the concentration front, and K_T is the longitudinal dispersion coefficient.

The same channel configuration as Section 4.2.1 was used to simulate this situation with a K_T of 30.0. The channel was given an initial concentration of zero, and a constant concentration of 10.0. Also, as in Section 4.2.1, three transport time steps were used to yield three Courant numbers: 0.1, 1.0, and 6.0.

As in Section 4.2.2, MASS2 exhibited noticeable numerical diffusion, smearing the front more than predicted by the analytic solution (Figure 4.25). The simulations at higher Courant numbers exhibited more diffusive behavior. Simulated concentrations were the same when using multiple blocks (Figure 4.26). The multi-block meshes used were the same as described in Section 4.1.1.

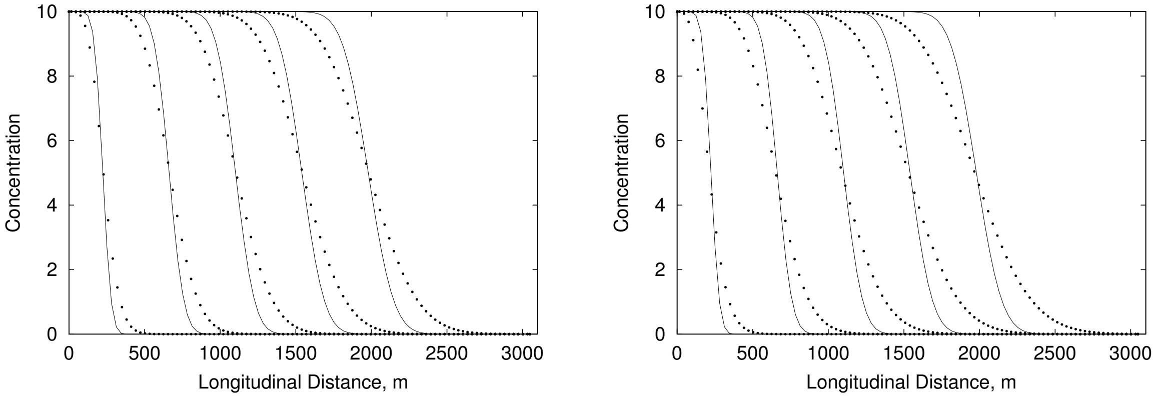

(a) $C_o = 0.1$ (b) $C_o = 1.0$

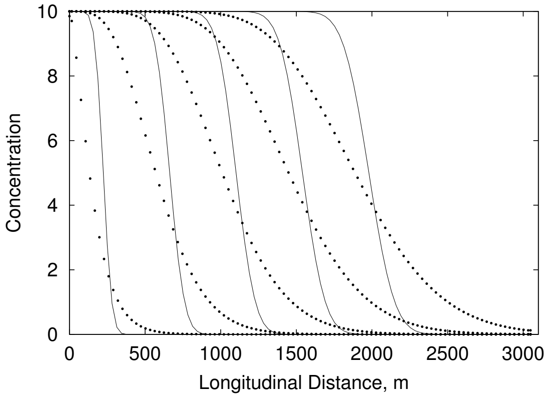

(c) $C_o = 6.0$

Figure 4.25. Simulated concentration (points) compared with the analytic solution (equation 4.4, solid line) to the one-dimensional advective diffusion test. Three cases are shown: (a) $C_o = 0.1$, (b) $C_o = 1.0$, and (c) $C_o = 6.0$. Concentration profiles are shown at 6-minute intervals, starting 6 minutes after the concentration peak was reached at the boundary.

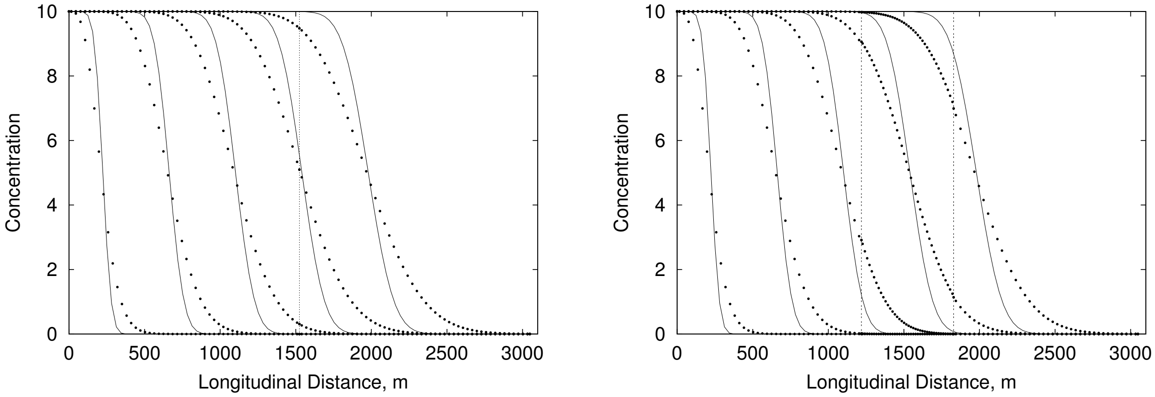

(a) (b)

Figure 4.26. Concentration from multi-block simulations (points) compared to the analytic solution (equation 4.4, solid line) to the one-dimensional advective diffusion test. Concentration profiles are shown at 6 minute intervals, starting 6 minutes after the concentration peak was reached at the boundary. Vertical lines indicate block boundaries. Simulation results are for $C_o = 1.0$.

4.2.3 Lateral Mixing

This test was used to check the MASS2 simulation of steady-state lateral mixing of a transported contaminant. A constant concentration, C_b, was applied along one half of the upstream boundary and a higher constant concentration, C_o, was applied along the other half. This problem has an analytic solution described by Fischer et al. (1979):

$$C(x,y) = \frac{C_o}{2}\sum_{n=-\inf}^{\inf}\left[\operatorname{erf}\left(\frac{y'+\frac{1}{2}+2n}{\sqrt{4x'}}\right)-\operatorname{erf}\left(\frac{y'-\frac{1}{2}+2n}{\sqrt{4x'}}\right)\right]+C_b \tag{4.5}$$

where $x' = \frac{x\varepsilon_t}{VW^2}$ and $y' = \frac{y}{W}$.

MASS2 was configured to simulate uniform flow with a depth of 1.83 m (6 ft) in a rectangular channel 30.4 m (100 ft) wide and 1219 m (4000 ft) long. A constant discharge of 56.6 m^3/sec (2000 cfs) was supplied as the upstream boundary condition, and a constant depth of 1.83 m was supplied as a downstream boundary condition. The longitudinal and lateral diffusivity (ε_1 and ε_2 in equation 2.8) were set to 0.279 m^2/sec (3.0 ft^2/sec). This value was also used for ε_t in the analytic solution.

A contour plot of simulated steady-state concentrations is shown in Figure 4.27. Simulated concentrations matched the analytic solution very well both laterally (Figure 4.28) and longitudinally (Figure 4.29).

4.2.4 Point Source

This case was used to compare the output of a MASS2 simulation of a contaminant species supplied to the channel as a point source with an analytic solution to the problem. The analytic

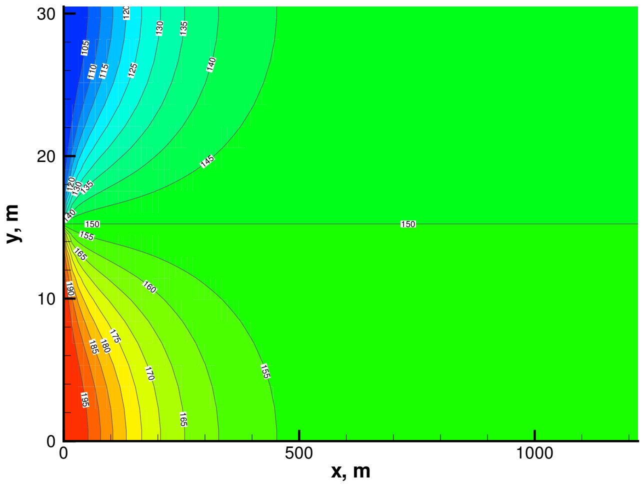

Figure 4.27. Contour plot of simulated concentration from the lateral mixing test.

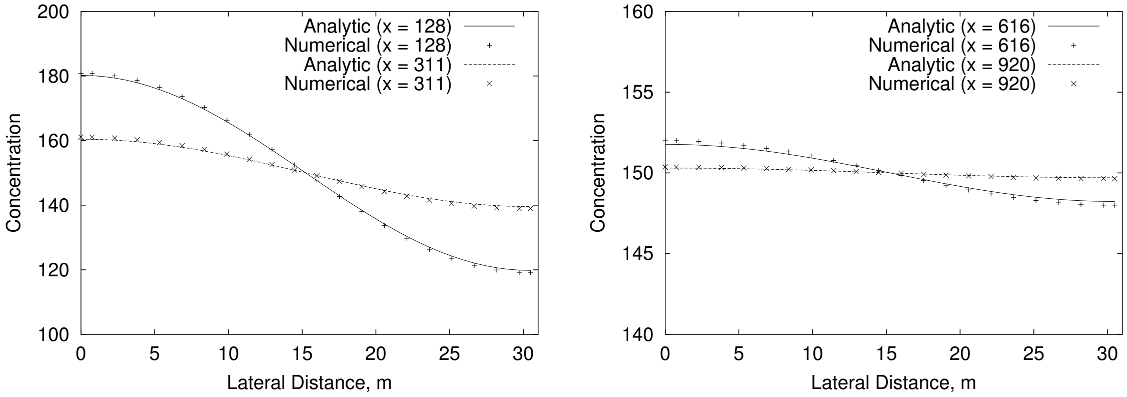

Figure 4.28. Lateral variation of simulated concentration compared with the analytic solution to the lateral mixing test.

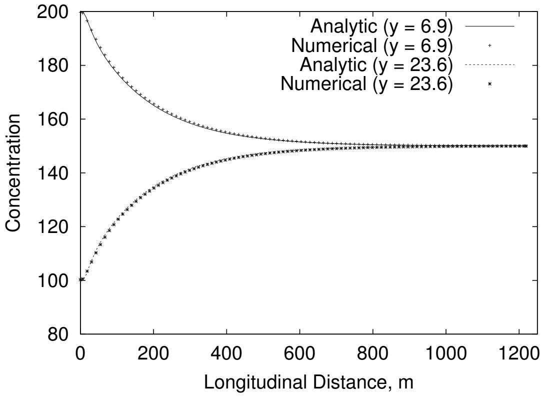

Figure 4.29. Longitudinal variation of simulated concentration compared with the analytic solution to the lateral mixing test.

solution, from Fischer et al. (1979), is

$$\frac{C}{C_o} = \frac{1}{(4\pi x')^{\frac{1}{2}}} \sum_{n=-\inf}^{\inf} \left\{ \exp\left[-\left(y' - 2n - y'_o\right)^2 / 4x'\right] + \exp\left[-\left(y' - 2n + y'_o\right)^2 / 4x'\right] \right\} \tag{4.6}$$

where

$$C_o = \frac{\dot{M}}{VdW}, \quad x' = \frac{x\varepsilon_t}{VW^2}, \quad \text{and} \quad y' = \frac{y}{W}$$

and $\left(x^o, y^o\right)$ is the location of the source, and $\dot{M}$ is the mass source rate.

MASS2 was configured to simulate the channel described in Section 4.1.1 with a 200 by 25-cell mesh. A constant source of contaminant $\left(\dot{M} = 1.0 \text{ units/sec}\right)$ was supplied to a single cell near the upstream boundary. The center of the cell was located at x^o = 22.9 m (75 ft) and y^o = 38.1 m (125 ft). The longitudinal and lateral diffusivity (ε_1 and ε_2 in equation 2.8) were set to 0.019 m^2/sec (0.2 ft^2/sec). This value was also used for ε_t in the analytic solution.

A contour plot of the steady-state concentrations simulated is shown in Figure 4.30. MASS2 simulated concentrations close to the solution, except very near the source, where MASS2 over-estimated peak concentrations (Figure 4.31).

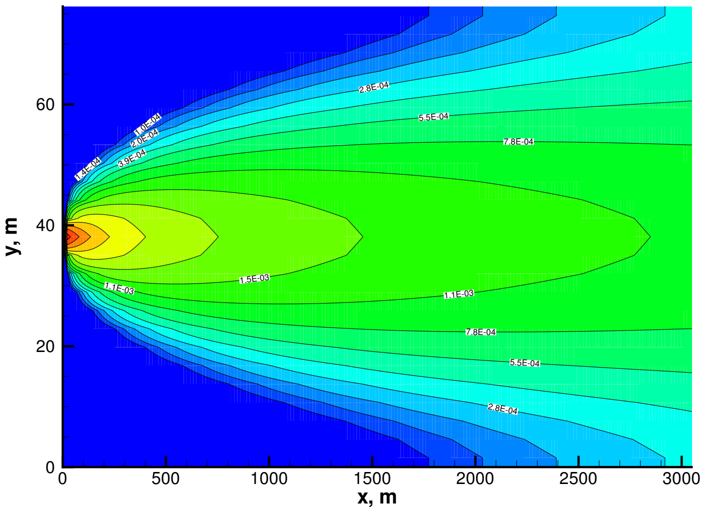

Figure 4.30. Contour plot of simulated concentration from the point source transport test.

4.2.5 Radioactive Decay

An analytic solution to compute concentrations of a decaying scalar quantity along the channel was presented by Fischer et al. (1979) as

$$C = C_o \exp\left[-\left(\frac{U_o x}{2K}\right)\left(\sqrt{\alpha + 1} - 1\right)\right] \tag{4.7}$$

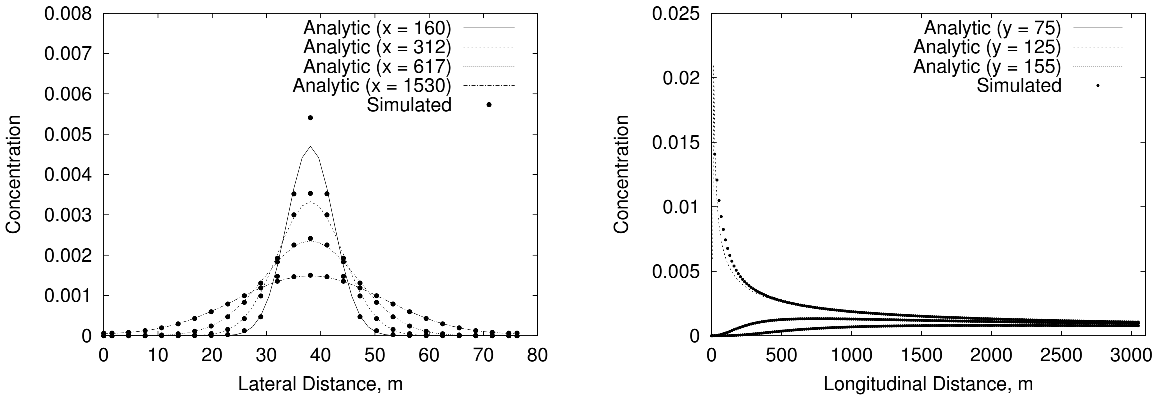

(a) (b)

Figure 4.31. Lateral (a) and longitudinal (b) variation of simulated concentration compared with the analytic solution to the point source test.

where K is a dispersion coefficient, U_o is the bulk velocity,

$$\alpha = \frac{4K\lambda}{U_o^2}, \tag{4.8}$$

and

$$C_o = C_i \left[\frac{2}{\alpha} \left(\sqrt{\alpha + 1} - 1 \right) \right] \tag{4.9}$$

MASS2 was configured to simulate the channel described in Section 4.1.1. A constant concentration of decaying contaminant, $C_i = 10.0$, was imposed as a boundary condition at the upstream end. The half-life of the contaminant was chosen to be the travel time in the channel,

$$\frac{3048 \text{ m}}{0.61 \text{ m/sec}} \; = \; 5000 \text{ sec, so that } \lambda \; = \; \frac{\log 2}{5000} \; = \; 1.386 \times 10^{-4}$$

and the expected concentration at the channel outfall would be precisely half the inflow concentration. Concentrations simulated were very close to the analytic solution and the simulate downstream concentration was half the inflow concentration (Figure 4.32).

4.2.6 Dissolved/Particulate Species Partitioning

This test was used to exercise the simulated exchange between dissolved and particulate phases of a scalar species. The simple rectangular channel and flow conditions in Section 4.1.1 was used. At the upstream boundary, clean sediment (particulate concentration was zero) was supplied at a concentration of 1.0, and purely dissolved contaminant was supplied at a concentration of 1.0. The partitioning coefficient, K_{d_ϕ}, was set to 1.0, so that, as the dissolved contaminant was transported downstream, it equilibrated with the sediment to the point were the dissolved and particulate concentrations were both 0.5. The transfer rate, K_ϕ, was set to 5×10^{-4} sec^{-1}.

As expected, simulated dissolved and particulate approached concentrations of 0.5 and nearly reached equilibrium at the channel outfall (Figure 4.33a). A second simulation was performed in

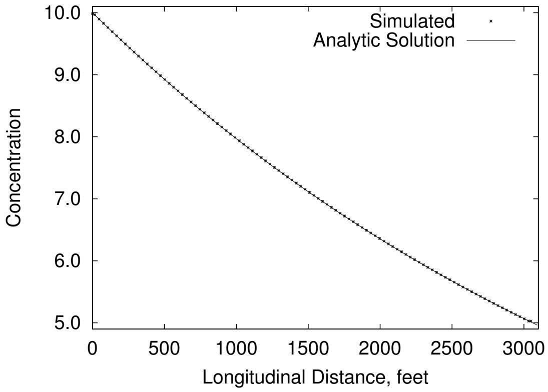

Figure 4.32. Simulated concentrations of a decaying scalar quantity compared with analytic solution.

which the contaminant was assigned a half-life of 5000 sec (reach travel time). MASS2 correctly simulated the decay in both phases, so that the concentrations at the channel outfall were half of the previous simulation (Figure 4.33b).

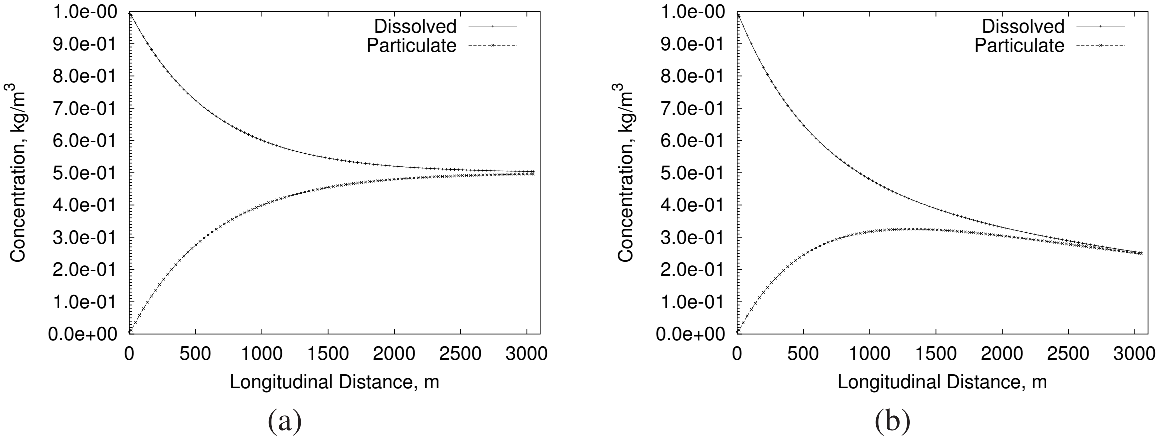

Figure 4.33. Simulated dissolved and particulate concentrations in the species partitioning test. The conservative contaminant case is shown in (a); (b) shows the decaying contaminant case.

5.0 Future Development

Following its original development, additional capabilities have been added to MASS2 to meet the specific needs of new applications. New code features which the authors plan to add (subject to available funding) include the following:

- Second-order time differencing
- Second-order monotonic scheme for advection
- SIMPLER and SIMPLEC velocity-depth coupling schemes to improve rate of convergence
- Depth-averaged turbulence model
- Multilayer sediment bed
- Bedload sediment transport
- Internal flow regulation in cells - culverts, weirs, flow over embankments
- Improved input file checking and error trapping
- Additional output file options and utilities

6.0 References

Balay S, K Buschelman, WD Gropp, D Kaushik, M Knepley, LC McInnes, BF Smith, and H Zhang. 2002. *PETSc Users Manual*. ANL-95/11 - Revision 2.1.5, Argonne National Laboratory.

Balay S, WD Gropp, LC McInnes, and BF Smith. 1997. “Efficient Management of Parallelism in Object Oriented Numerical Software Libraries.” In *Modern Software Tools in Scientific Computing*, Arge E, AM Bruaset, and HP Langtangen, eds., pp. 163–202. Birkhauser Press.

Brown L and T Barnwell, Jr. 1987. *The Enhanced Stream Water Quality Models QUAL2E and QUAL2E-UNCAS: Documentation and User Manual.* U.S. Environmental Protection Agency, Environmental Research Laboratory, Athens, GA. EPA/600/3-87/007.

Chang Y. 1971. *Lateral Mixing in Meandering Channels*. PhD thesis, University of Iowa, Iowa City, Iowa.

Chow V. 1959. *Open Channel Hydraulics*. McGraw-Hill, New York.

Colt J. 1984. *Computation of Dissolved Gas Concentrations in Water as Functions of Temperature, Salinity, and Pressure.* Report, American Fisheries Society, Bethesda, Maryland. Special Publication 14, ISBN 0-913235-02-4.

Duffie JA and WA Beckman. 1982. *Solar Energy Thermal Processes*. John Wiley and Sons, New York.

Edinger JE, DK Brady, and JC Geyer.. 1974. *Heat Exchange and Transport in the Environment.* Publication No. 74-049-003, Electric Power Research Institute (EPRI), Palo Alto, CA. Publication No. 74-049-003.

Falconer RA and Y Chen. 1991. “An improved representation of flooding and drying and wind stress effects in a two-dimensional tidal numerical model.” *Proceedings of the Institution of Civil Engineers* 91:659–678.

Fischer H, EJ List, R Koh, J Imerger, and N Brooks. 1979. *Mixing in Inland and Coastal Waters.* Academic Press, New York, New York.

Gates DM. 1980. *Biophysical Ecology*. Springer-Verlag, New York.

Gharangik AM. 1988. “Numerical simulation of hydraulic jump.” Master’s thesis, Washington State University, Pullman, Washington.

Kincaid CT, RW Bryce, PW Eslinger, CAB J. M. Becker, AL Bunn, CR Cole, EJ Freeman, GR Guensch, DG Horton, GV Last, TB Miley, WA Perkins, WE Nichols, M Oostrom, MC Richmond, DL Strenge, and PD Thorne. 2001. “Development of a Site-Wide System Assessment Capability.” Presented at the Waste Management 2001 Symposium, February 25 - March 1, 2001, sponsored by the University of Arizona, Tuscon, Arizona.

Klonidis AJ and JV Soulis. 2001. “An Implicit Scheme for Steady Two-Dimensional Free-Surface Flow Calculation.” *Journal of Hydraulic Research* 39(4):393–402.

Krone RB. 1962. *Flume Studies of the Transport of Sediment in Estuarial Shoaling Processes*. Hydraulic Engineering and Sanitary Engineering Research Laboratory, University of California, Berkeley, California.

MacDonald I, MJ Baines, NK Nichols, and PG Samuels. 1997. “Analytic Benchmark Solutions for Open-Channel Flows.” *Journal of Hydraulic Engineering* 123(11):1041–1045.

McMichael GA, WA Perkins, CJ McMurray, YJ Chien, CL Rakowski, A Coleman, MC Richmond, J Vucelick, EV Arntzen, RP Mueller, CA Duberstein, and J Lukas. 2003. *Subyearling Chinook Salmon Stranding in the Hanford Reach of the Columbia River*. PNWD-3308, Battelle-Pacific Northwest Division, P.O. Box 999, Richland, Washington 99352. Prepared for Grant County Public Utility District No. 2.

Molls T and MH Chaudhry. 1995. “Depth-Averaged Open-Channel Flow Model.” *Journal of Hydraulic Engineering* 121(6):453–465.

Molls T, MH Chaudhry, and KW Khan. 1995. “Numerical Simulation of Two-Dimensional Flow Near a Spur-Dike.” *Advances in Water Resources* 18(4):227–236.

Monteith JL and MH Unsworth. 1990. *Principles of Environmental Physics*, second edition. Edward Arnold, London.

Nawachukwu BA. 1979. *Flow and Erosion Near Groyne-Like Structures*. PhD thesis, University of Alberta, Alberta, Canada.

Norris SE. 2000. *A Parallel Navier-Stokes Solver for Natural Convection and Free Surface Flow*. PhD thesis, Department of Mechanical Engineering, University of Sydney.

O’Connor D. 1982. “Wind Effects on Gas-Liquid Transfer Coefficients.” *Journal of Environmental Engineering* 109(3):731–752.

Onishi Y and FL Thompson. 1984. *Mathematical Simulation of Sediment and Radionuclide Transport in Coastal Waters, Volume 1: Testing of the Sediment/Radionuclide Transport Model, FETRA*. PNL-5088-1, NUREG/CR-2424, Pacific Northwest Laboratory, Richland, Washington 99352. Prepared for the U.S. Nuclear Regulatory Commission.

Ouillon S and D Dartus. 1997. “Three-Dimensional Computation of Flow Around Groyne.” *Journal of Hydraulic Engineering* 123(11):962–970.

Panagiotopoulos AG and JV Soulis. 2000. “Implicit Bidiagonal Scheme for Depth-Averaged Free-Surface Flow Equations.” *Journal OF Hydraulic Engineering* 126(6):425–436.

Partheniades E. 1962. *A Study of Erosion and Deposition of Cohesive Soils in Salt Water*. PhD thesis, University of California, Berkeley, California.

Patankar S. 1980. *Numerical Heat Transfer and Fluid Flow.* Hemisphere, New York, New York.

Perkins W, M Richmond, and G McMichael. 2004. "Two-Dimensional Modeling of Time-Varying Hydrodynamics and Juvenile Chinook Salmon Habitat in the Hanford Reach of the Columbia River." In *Proceedings of the World Water and Environmental Resources Congress*. ASCE. Presented at conference held June˜ 27-July˜ 1 in Salt Lake City.

Perkins WA and MC Richmond. 2004. *MASS2, Modular Aquatic Simulation System in Two Dimensions, User Guide and Reference*. PNNL-14820-2, Pacific Northwest National Laboratory, Richland, Washington 99352.

Rajaratnam N and Nwachukwu. 1983. "Flow Near Groyne-like Structures." *Journal of the Hydraulics Engineering* 109(3):463–480.

Richmond M, H Chen, and V Patel. 1986. *Equations of Laminar and Turbulent Flows in General Curvilinear Coordinates.* Institute of Hydraulic Research, University of Iowa, Iowa City, IA. IIHR Report No. 300.

Richmond M, W Perkins, and Y Chien. 2000. *Numerical Model Analysis of System-wide Dissolved Gas Abatement Alternatives*. PNWD-3245, Battelle Pacific Northwest Division, P.O. Box 999, Richland, Washington, 99352. Prepared for the U.S. Army Corps of Engineers, Walla Walla District under Contract DACW68-96-D-0002.

Richmond M, W Perkins, and C Rakowski. 1999a. *Two-Dimensional Analysis of Flow Conditions and Sediment Mobility in the Lower Snake River for Impounded and Natural River Conditions*. U.S. Department of Energy, Pacific Northwest National Laboratory, P.O. Box 999, Richland, Washington. Prepared for the U.S. Army Corps of Engineers, Walla Walla District.

Richmond M, W Perkins, and T Scheibe. 1999b. "Two-Dimensional Hydrodynamic, Water Quality, and Fish Exposure Modeling of the Columbia and Snake Rivers." In *WaterPower Conference*. Las Vegas, NV.

Rodi W and K Weiss. 1980. *Laboruntersuchungen des Nahfelds vod Warmwassereinleitungen in Rechteckgerinne*. Report No. 574, Institute for Hydromechanics, University of Karlsrube, Germany. (in German).

Shyy W, S Thakur, H Ouyang, J Liu, and E Blosch. 1997. *Computational Techniques for Complex Transport Phenomena*. Cambridge University Press.

Thakur S, J Wright, W Shyy, and H Udaykumar. 1997. *SEAL, A Computational Fluid Dynamics and Heat Transfer Code for Complex 3D Geometries Theory, Implementation and User's Manual, Version 2.1*. Aerospace Engineering, Mechanics and Engineering, Science Department, University of Florida, Gainesville, Florida. Available URL: `http://www.aero.ufl.edu/˜cfdweb/seal1.html`.

Tingsanchali T and S Maheswaran. 1990. "2-D Depth-Averaged Flow Computation near Groyne." *Journal of Hydraulic Engineering* 116(1):71–86.

Tuminaro RS, M Heroux, SA Hutchinson, and JN Shadid. 1999. *Official Aztec User's Guide*. Massively Parallel Computing Research Laboratory, Sandia National Laboratories, Alburqueryque, New Mexico 87185. Available URL:˜ `http://www.cs.sandia.gov/CRF/aztec1.html`.

Versteeg HK and W Malalasekera. 1995. *An Introduction to Computational Fluid Dynamics, the Finite Volume Method*. Prentice-Hall.

Wigmosta M and W Perkins. 1997. *A GIS-based Modeling System for Watershed Analysis.* Battelle Pacific Northwest Division, P.O. Box 999, Richland, Washington, 99352. Report to the National Council of the Paper Industry for Air and Stream Improvement (NCASI), Weyerhaeuser Co., and MacMillan Bloedel Limited.

Ye J and JA McCorquodale. 1997. "Depth-Averaged Model in Curvilinear Collocated Grid." *Journal of Hydraulic Engineering* 123(5):380–388.

Zhou JG. 1995. "Velocity-Depth Coupling in Shallow-Water Flows." *Journal of Hydraulic Engineering* 121(10):717–724.